

SAHA, SUJOY, M.S. Synthesis, Characterization and Understanding Photophysical Properties of Isorecticular Metal-Organic Frameworks. (2021)

Directed by Dr. Hemali Rathnayake. 71 pp

A series of isorecticular metal-organic frameworks (IRMOFs) formed by self-assembly directed solvothermal process using organic chromophores with metal ions emerge as future luminophores for optoelectronic devices. We have explored the photophysical properties of IRMOFs, consisting of different ligands of dicarboxylic acids, as luminophores. The crystalline cubic structures of IRMOFs with rigid frameworks of dicarboxylic acid units exhibit solvent-driven charge transfer dynamics, investigated from the photoluminescence intensity and peak shift in emission spectra of IRMOFs in different solvents. The elemental composition analysis confirms the original structural formulas of n-IRMOFs, where n= 1, 8, and 10. The thermal stability and dielectric properties of IRMOFs are also explored. A rapid analytical approach combining experimental spectroscopic data with theoretical equations is developed to predict the electronic band structure of these three IRMOFs by considering a 1-D periodic array model. This novel analytical approach serves as a predictive and rapid screening tool to search the MOF database to identify potential semiconducting MOFs.

SYNTHESIS, CHARACTERIZATION AND UNDERSTANDING PHOTOPHYSICAL  
PROPERTIES OF ISORETICULAR METAL-ORGANIC FRAMEWORKS

by

Sujoy Saha

A Thesis

Submitted to

the Faculty of The Graduate School at

The University of North Carolina at Greensboro

in Partial Fulfillment

of the Requirements for the Degree

Master of Science

Greensboro

2021

Approved by

Dr. Hemali Rathnayake

Committee Chair

APPROVAL PAGE

This thesis written by Sujoy Saha has been approved by the following committee of the Faculty of The Graduate School at The University of North Carolina at Greensboro.

Committee Chair      Dr. Hemali Rathnayake

Committee Members      Dr. Joseph Starobin

Dr. Tetyana Ignatova

Dr. Jeffery Alston

4/20/2021

Date of Acceptance by Committee

4/20/2021

Date of Final Oral Examination

## ACKNOWLEDGEMENTS

I would like to express my gratitude to my advisor Dr. Hemali Rathnayake for her time, expertise, and support with this project and my graduate studies in general. With her supervision, I have become a more competent and critical researcher. Additionally, I want to thank Dr. Joseph Starobin, Dr. Tetyana Ignatova, and Dr. Jeffery Alston for their time serving as my committee members. I would also like to thank the Joint School of Nanoscience and Nanoengineering (JSNN). Besides, JSNN staff supported me with their advice, training, and equipment troubleshooting, particularly Dr. Kyle Nowlin and Dr. Md. Jamal Uddin. I want to acknowledge the following peers for experimental and computational assistance; Gayani Pathiraja, Shane Loeffler, and the rest of the Dr. Hemali group. Thanks to my parents and wife for their unconditional support throughout my academic and personal journeys.

## TABLE OF CONTENTS

LIST OF TABLES .....	vii
LIST OF FIGURES .....	viii
CHAPTER I: INTRODUCTION.....	1
1.1 Overview .....	1
1.2 Research Goal .....	2
CHAPTER II: BACKGROUND .....	4
2.1 Metal-Organic Frameworks (MOFs) .....	4
2.1.1 Isorecticular Metal-Organic Frameworks (IRMOFs) .....	4
2.2 Photophysical Properties.....	5
2.3 Dielectric Constant.....	6
2.4 State-of-the-Art .....	7
2.4 Theoretical Background.....	11
2.4.1 Analytical Approach to Predict Band Structure.....	11
2.4.2 Implement of Bloch Theorem .....	12
CHAPTER III: EXPERIMENTAL PROCEDURES.....	15
3.1 Synthesis of Isorecticular Series of $Zn_4O(L)_3$ MOFs .....	15
3.1.1 Reaction Scheme for the Synthesis Route of IRMOFs:.....	15
3.2 Synthesis Method.....	15
3.2.1 Synthesis of IRMOF-8.....	16
3.2.2 Synthesis of IRMOF-10.....	16
3.2.3 Synthesis of IRMOF-1 .....	17
3.3 Dielectric Properties.....	18

3.3.1 Capacitor type Device Making .....	18
3.3.2 Capacitance Measurement .....	19
3.3.3 Thickness Measurement.....	19
3.4 Photophysical Properties.....	19
3.4.1 UV-Vis Analysis .....	19
3.4.2 PL Analysis .....	19
3.4.3 Solvent-Dependent Charge Transfer Dynamics Studies.....	20
3.5 The Technique to Predict Band Structures .....	20
3.5.1 Considering only Metal Nodes .....	20
3.5.2 Considering the Organic Ligands with Metal Nodes.....	22
3.5.3 Calculations for Plotting Energy Curve.....	22
3.5.4 E vs $\kappa a$ for Showing Allowed Energy Bands.....	23
CHAPTER IV: RESULTS AND DISCUSSION .....	24
4.1 Chemical Composition.....	24
4.1.1 Functional Groups by FTIR .....	24
4.1.2 Chemical Composition, Oxidation States, and Chemical Environment by XPS.....	25
4.2 Morphologies of IRMOFs.....	28
4.3 Structural Properties by XRD .....	29
4.4 Photophysical Properties.....	32
4.4.1 Absorption and Emission Spectra for Band Structure .....	32
4.4.2 Solvent-Dependent Photoluminescence Emission.....	34
4.5 Thermal Stability .....	38
4.6 Dielectric Properties.....	42
4.6.1 Thin-Film Thickness Measurement from SEM .....	42
4.6.2 Dielectric Constant Calculation .....	42

4.7 $\beta$ Calculation Considering Only Metal Nodes .....	45
4.7.1 $\beta$ for IRMOF-8 (Zn-NDC MOF) .....	45
4.7.2 $\beta$ for IRMOF-10 (Zn-BPDC MOF) .....	46
4.7.3 $\beta$ for IRMOF-1 (Zn-BDC MOF) .....	47
4.8 Mapping Energy Band Structures for IRMOFs .....	49
4.8.1 Predicting Energy Band Structures Considering Only Metal Nodes.....	49
4.8.2 Mapping Energy Band Structures with the Impact of Organic Parts.....	51
4.9 Energy Band Diagrams for IRMOFs .....	53
4.9.1 IRMOF-8.....	53
4.9.2 IRMOF-10.....	54
4.9.3 IRMOF-1.....	55
4.10 Energy Curves.....	56
4.10.1 Calculations for Energy Curve.....	56
4.10.2 E vs $\kappa a$ for Showing Allowed Energy Bands.....	56
CHAPTER V: CONCLUSION.....	60
REFERENCES .....	62
APPENDIX A: MATLAB PROGRAMMING .....	70

## LIST OF TABLES

Table 1: Dielectric Constant Calculation from Capacitance for IRMOF-8.....	43
Table 2: Dielectric Constant Calculation from Capacitance for IRMOF-10.....	43
Table 3: Dielectric Constant Calculation from Capacitance for IRMOF-1.....	44
Table 4: $\epsilon$ & $\beta$ Values of IRMOFs.....	48
Table 5: $\beta$ for All IRMOFs Considering the Organic Parts.....	51



## LIST OF FIGURES

Figure 1: Schematic Diagram of Metal-Organic Framework (MOF).....	4
Figure 2: 1-D Array of Zn Metal Nodes and Corresponding Periodic Delta Function .....	12
Figure 3: Graph of $f(z)$ vs. $z$ Showing Allowed Bands and Energy Gaps <sup>70</sup> .....	14
Figure 4: Schematic Diagram of Dielectric Capacitor.....	18
Figure 5: FTIR for IRMOF-1 .....	24
Figure 6: XPS of IRMOF-1: (a) XPS survey, (b) Zn 2p, (c) C 1s, and (d) O 1s .....	25
Figure 7: XPS of IRMOF-8: (a) XPS survey, (b) Zn 2p, (c) C 1s, and (d) O 1s .....	26
Figure 8: XPS of IRMOF-10: (a) XPS survey, (b) Zn 2p, (c) C 1s, and (d) O 1s .....	27
Figure 9: SEM of IRMOF-8 (top left), IRMOF-10 (top right), and IRMOF-1(bottom) .....	29
Figure 10: XRD Spectrum of IRMOF-8 (Experimental and Simulated) <sup>77</sup> .....	30
Figure 11: XRD Spectrum of IRMOF-10 (Experimental and Simulated).....	31
Figure 12: XRD Spectrum of IRMOF-1 (Experimental and Simulated).....	32
Figure 13: UV-Vis (left) & PL-Analysis (right) for IRMOF-8 .....	33
Figure 14: UV-Vis (left) & PL-Analysis (right) for IRMOF-10 .....	33
Figure 15: UV-Vis (left) & PL-Analysis (right) for IRMOF-1 .....	34
Figure 16: PL Emission Spectra of IRMOF-8 in Five Different Polar Solvents .....	35
Figure 17: PL Emission Spectra of IRMOF-1 in Five Different Polar Solvents .....	36
Figure 18: PL Emission Spectra of IRMOF-10 in Five Different Polar Solvents .....	37
Figure 19: TGA for IRMOF-1 .....	39
Figure 20: TGA for IRMOF-8 .....	40
Figure 21: TGA for IRMOF-10 .....	41
Figure 22: SEM Image of the Cross-Sectional Part of the Device .....	42
Figure 23: Comparing $\epsilon$ Values (from left to right: IRMOF-8, IRMOF-10, IRMOF-1).....	44
Figure 24: Energy Bands of IRMOF-8 Without Considering Organic Part .....	49
Figure 25: Energy Bands of IRMOF-10 Without Considering Organic Part .....	50

Figure 26: Energy Bands of IRMOF-1 Without Considering Organic Part .....	50
Figure 27: Energy Bands of IRMOF-8 Considering Organic Part (Dielectric Substance).....	52
Figure 28: Energy bands of IRMOF-10 Considering Organic Part (Dielectric Substance) .....	52
Figure 29: Energy bands of IRMOF-1 Considering Organic Part (Dielectric Substance) .....	53
Figure 30: Energy Band Diagram for IRMOF-8 .....	54
Figure 31: Energy Band Diagram for IRMOF-10 .....	55
Figure 32: Energy Band Diagram for IRMOF-1 .....	55
Figure 33: Energy Curve for IRMOF-8 .....	57
Figure 34: Energy Curve for IRMOF-10 .....	57
Figure 35: Energy Curve for IRMOF-1 .....	58
Figure 36: Comparing Energy Curves (Blue: IRMOF-8, Green: IRMOF-1, Red: IRMOF-10) ..	58

## CHAPTER I: INTRODUCTION

### *1.1 Overview*

The extensive possible combination of the inorganic metal nodes and organic ligands as building blocks of thousands of Metal-Organic Frameworks (MOFs) structures has been created. Many MOFs have been synthesized, functionalizing the organic linker.<sup>1</sup> Very few experimental and computational studies have been conducted on MOFs, either functionalizing the organic linker or varying the metallic oxide cluster.<sup>2,3,4</sup> MOFs have been explored widely as a promising novel area of functional luminescent materials. Luminescence properties of MOFs can arise from the direct emission of the organic linkers, emission of transition-metal centered, and the interactions between the organic chromophore and the metal node via charge transfer processes between ligands and metals, which include either Ligand-to-Metal Charge Transfers (LMCT) or Metal-to-Ligand Charge Transfers (MLCT).<sup>5</sup>

Around 90,000 MOFs have already been synthesized, and more than 500,000 MOFs are predicted.<sup>6</sup> Among all MOFs, luminescent MOFs have emerged as developing materials that combine light emission with the properties of porosity, magnetism, chirality, molecule, and ion sensing, catalysis, and activity as multimodal imaging contrast agents.<sup>7</sup> Nanoporous MOFs have potential applications in gas storage, gas separation, and catalysis because of its prudent options of organic linkers and unique structural features of MOFs such as pore size, shape, and chemical functionality.<sup>8,9,10</sup>

Thus, MOFs have attained significant research interest. Among them, isorecticular MOFs (IRMOFs) have been abundantly studied because of their simple synthesis and potential applications.<sup>11</sup>

MOF-5, also known as IRMOF-1, is one of the well-studied MOF structures, the first MOF in the series of isorecticular MOFs, represented by the formula  $M_4O(L)_3$ , where  $M = Zn$  and the organic ligand  $L = \text{benzene-1,4-dicarboxylic acid (BDC)}$ . It is the template for constructing the series of isorecticular MOFs (IRMOFs-n, where  $n = 1-8, 10, 12, 14, \text{ and } 16$ ).<sup>12</sup> Here, three different IRMOFs are synthesized and characterized, the solvent-dependent charge transfer dynamics of IRMOFs are investigated, and band structures are predicted.

## ***1.2 Research Goal***

The research goal is to understand the photophysical and dielectric properties of three different IRMOFs with respect to the conjugation length of the organic linker while keeping the same metal node.

Aim 1: Synthesis and characterization of three isorecticular MOFs with  $Zn_4O(L)_3$  formula

Task 1: Synthesis of IRMOF-1 (or MOF 5), IRMOF-8, and IRMOF-10 using Zinc acetate and Benzene-1, 4-dicarboxylic acid (BDC), 2, 6-Naphthalene dicarboxylic acid (NDC), and Biphenyl-4, 4'- dicarboxylic acid (BPDC), respectively

Task 2: Studying morphological, compositional, structural, and dielectric properties of IRMOF-1, IRMOF-8, and IRMOF-10

Aim 2: Understanding photophysics of the isorecticular series of  $Zn_4O(L)_3$  MOFs

Task 1: Studying photophysical properties of three IRMOFs in different solvents

Task 2: Predicting energy band diagrams for the three IRMOFs

## CHAPTER II: BACKGROUND

### 2.1 Metal-Organic Frameworks (MOFs)

Metal-organic framework is a hybrid crystalline porous structure of organic and inorganic components shown in Figure 1, which is self-assembled from the organic ligands and inorganic metal nodes. This type of framework is included as a subclass of the co-ordination network, one of the co-ordination polymer subsets.<sup>13</sup> According to IUPAC, MOF is a co-ordination network where organic ligands contain potential voids.<sup>14</sup> In literature, MOFs are mentioned by using several terminologies such as metal-organic material (MOM), porous co-ordination network (PCN), co-ordination polymer (CP), microporous co-ordination polymer (MCP), and metal-organic co-ordination network (MOCN).<sup>15</sup>

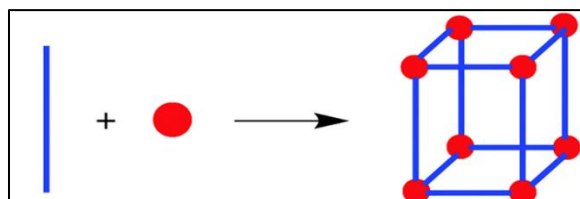


Figure 1: Schematic Diagram of Metal-Organic Framework (MOF)

#### 2.1.1 Isoreticular Metal-Organic Frameworks (IRMOFs)

IRMOFs show similar crystal structures consisting of zinc-based metal oxide clusters and benzene carboxylate-based organic linkers.<sup>16</sup> All IRMOFs have the presumed topology of cubic  $\text{CaB}_6$  modified by the prototype IRMOF-1, an oxide-centered  $\text{Zn}_4\text{O}$  tetrahedron, and edge-bridged six carboxylates to give the octahedron-shaped secondary building unit (SBU) that reticulates into the

3-D cubic porous network. In IRMOF-2 through IRMOF-7, benzene dicarboxylic acid (BDC) links with six separate functional groups. IRMOF-8 through -16 have progressively longer links where BPDC linkers in IRMOF-9 and IRMOF10 are reticulated as like as doubly interpenetrating structures.<sup>17,18,19</sup>

Among all IRMOFs, IRMOF-1 and IRMOF-8 have been widely studied for gas-sorption and storage applications.<sup>20</sup> MOFs as thin films have advanced optical<sup>21</sup>, electronic, and magnetic applications.<sup>16,22</sup>

## ***2.2 Photophysical Properties***

Electronically excited states play one of the most vital roles in different materials and chemical engineering, organic chemistry, and condensed matter physics.<sup>23</sup> Photophysical properties describe the compound's photoexcitation, absorption, and emission energy, not involving any chemical change. Organic functional materials have many applications compared with inorganic materials because of their less complicated processing and tunability of properties through a simple modification of their chemical reaction.<sup>24</sup>

Photophysical properties such as excited-state emissive lifetime and emission intensity of organic ligands in MOFs are generally different from those properties of the free molecules. It occurs as locked organic linkers in the MOF structure, reducing the nonradiative decay rate, leading to higher quantum efficiencies, fluorescence intensity, and lifetimes.<sup>25</sup> Very few research works have been conducted to evaluate the photophysics of IRMOFs series along with their luminescence behavior. Here, we assessed the photophysical properties of Zn<sub>4</sub>O-based IRMOFs.

### ***2.3 Dielectric Constant***

The dielectric constant, also termed the permittivity ( $\epsilon$ ), describes the material's interaction with an electric field. The dielectric constant ( $k$ ) is also known as relative permittivity ( $\epsilon_r$ ), which is the absolute permittivity ( $\epsilon$ ) relative to the permittivity of free space ( $\epsilon_0$ ). There is two part for the permittivity of a material. This permittivity's fundamental role is measuring the amount of energy stored in material from an external source of the electric field. The imaginary part of this permittivity is the loss factor, which calculates how dissipative material is in the electric field's external source. However, the dielectric constant is neither a function of frequency nor temperature. The relative lossiness of material is also known as tangent loss, and it is the ratio of lost energy to stored energy.

The dielectric constant was calculated by creating a capacitor-type device. A capacitor is a charge storage type device that stores the electric field's electric charge. This is a passive electronic component that has two terminals. Capacitance,  $C_p$  is measured from this type of device.  $C_p$  is the ratio of the charge (electric) amount stored on a conductor to a difference in electric potential. Nowadays, capacitors are used in electronic circuits for blocking the direct current while allowing the alternating current to pass through. the formulae to find dielectric constant

$$\epsilon = \frac{tC_p}{SK_0}$$

Where  $\epsilon$  is the dielectric constant,  $t$  is the thickness of thin-film,  $C_p$  is the capacitance of the device, and  $S$  is the capacitor zone's surface area.<sup>26</sup>



## ***2.4 State-of-the-Art***

Around 15% of synthetically known MOFs exhibit luminescence properties. The percentage is increasing tremendously in recent years<sup>27,28</sup> because of their potential application in light-emitting and display devices, fluorescent sensors,<sup>29,30</sup> nonlinear optics, electroluminescent devices,<sup>31,32</sup> photocatalysis, and biomedical imaging.<sup>33-35</sup> MOFs with large organic chromophore groups-porphyrin, pyrene, and others, have been investigated for the efficient exciton hopping and large exciton displacement within the framework.<sup>36-39</sup> Deria et al. reported a series of porphyrin-based MOFs and their emissive properties depending on framework topology.<sup>40</sup>

Lee et al. prepared Cu-based MOF films using a layer-by-layer (LBL) technique investigated as a light-absorbing layer in TiO<sub>2</sub>-based solar cells.<sup>41</sup> Zhang et al. created an optical sensing motif based on an electrodeposited luminescent Europium-thiophene-2,5-dicarboxylate (Eu-TDC) MOF thin film by the optimization of the parameters, which were used for the electrodeposition process. This thin film shows luminescence properties with the characteristic of Eu<sup>3+</sup>, which is sensitized by the electron-rich ligands.<sup>7</sup> Li et al. showed that when they implemented the reversible photochromism from bright yellow to dark green, the photochromic component of m-benzene dicarboxylate organic linker of Tb-BDC MOF can modulate the luminescence properties of the tetranuclear terbium cluster under irradiation of UV light. They defined this as photoluminescence switching behavior.<sup>42</sup> Wen et al. showed that IRMOF-3, where BDC links with an amino-functional group as the organic linker, could be a potential luminescent probe for detecting nitrobenzene or 2-nitrotoluene via fluorescence enhancement. They evaluated this MOF as a promising visible-light-driven photocatalyst for the degradation of organic pollutants.<sup>43</sup>

Hu et al. developed a novel Zn-MOF-based photochromic complex showing tunable photophysical behavior. They used viologen diacetic acid dichloride and BTEC as their organic ligands. They utilized suitable molecular self-assembly of luminophore and photochromic components to control luminescent emission in a single compound. They showed that a stable Zn-MOF structure provides a durable donor-acceptor framework with photo-stimulus luminescence patterning, reversible luminescence switching, and nondestructive readout of the luminescence signal.<sup>44</sup> Farahani et al. revealed microporous azine functionalized MOF, TMU-16 as the first example of MOF-based luminescent sensor and efficient multifunctional fluorescence material which can be used as selective sensing of ions such as Fe(III) and Cd(II) and small molecules such as CH<sub>2</sub>Cl<sub>2</sub>.<sup>45</sup>

Ding et al. showed their approach to fabricate energy-transfer MOF for ratiometric peroxynitrite (ONOO<sup>-</sup>) sensing. They quenched the bright blue fluorescence of MOF while the green or red emission from the acceptor is enhanced to increase the efficiency of FRET.<sup>46</sup> Tan et al. demonstrated the potential of MOF in the establishment of self-assembled FRET for developing ratiometric fluorescent nanoprobe. They used zeolitic imidazolate framework-8 as a MOF model to entrap carbon dot (CD) and curcumin (CCM) during its self-assembly.<sup>47</sup>

Stavila et al. focused on the basic requirements and structural elements to fabricate MOF-based devices and showed the current state of MOF research in the area of electronic, optoelectronic, and sensor devices.<sup>48</sup> Gan et al. developed a Cu-TCPP MOF nanosheets-based FRET autosensing platform to detect antibiotics. They found that Cu-TCPP nanosheets have an excellent affinity and quenching ability for novel hairpin probes and the SYBR Green complex.<sup>49</sup> Zhou et al. discussed the recent research advancements in using nanomaterials as donors and acceptors in FRET sensors. They showed the potential for Cu-MOFs and other 2-D nanomaterials in FRET sensing applications.<sup>50</sup>

Very few researches had been done to predict or calculate the electronic band structures of the Metal-Organic Framework (MOF).<sup>51,52,53</sup> Most of the researchers formulated the band structures by the computational method and estimated the band gaps from the experimental method via optical spectroscopy. But no research was done to tailor the band structure by using experimental parameters and theoretical calculations. Some research had done experimentally to check the impacts of the organic linkers of MOF on their electronic properties.<sup>54,55,56</sup>

Physicist Yablonovitch did a series of experimental and theoretical searches for the elusive photonic bandgap structures and summarized the similarities and the differences between photonic and electronic band structures.<sup>57</sup> Yablonovitch et al. introduced a new face-centered-cubic dielectric structure that simultaneously solves two of the photonic band structure's significant problems. They predicted the application of photonic band gaps to semiconductor physics, optical, and atomic physics, which might be practical.<sup>51</sup>

Pham-Tran et al. engineered the bandgap in MOFs by functionalizing organic linkers. They investigated the electronic band structures of a series of isorecticular MOFs (IRMOFs) and estimated bandgap from predicted HOMO– LUMO Energy for IRMOFs. They assessed bandgap experimentally, but no research had been done to check the band gap from the theoretical predictions for any type of MOFs up to date.

Wu et al. modulated the functionalized MOF's electronic band gaps where metal was Zirconium (Zr). Organic linkers were benzene- 1, 4- dicarboxylic acid (BDC) with different branched groups, i.e., H, NO<sub>2</sub>, and NH<sub>2</sub>. They calculated the UV-Vis bandgap from UV-Vis Cutting Edge and showed that bandgap is minimum for MOF with organic linker NH<sub>2</sub>-BDC as it has the maximum improvement in the light absorption.<sup>56</sup>

Using Discrete Fourier Transform (DFT), Liljeroth et al. calculated electronic band structures of two honeycomb MOFs with Cobalt metal and different linkers Dicyanobiphenyl (DCBP) and Dicyanoanthracene (DCA). They summarized that MOF with DCBP linker only has weak coupling between the building blocks and MOF. DCA linker shows in-plane hybridization, resulting in 2D electronic states with significant bandwidth.<sup>53</sup> But there are some overestimate and underestimate issues in the DFT method when predicting band structures.

Gascon et al. determined bandgap energies of MOFs with different organic dicarboxylic acid linkers by UV-Vis spectroscopy. They demonstrated that varying the metal incorporated in the MOF structure with the organic linker, benzene dicarboxylic acid (BDC), had little impact on the bandgap (around 3.5 eV). They showed the highest bandgap (4 eV) for MOFs with BDC linker and lowest (3.3 eV) for MOFs with naphthalene dicarboxylic acid (NDC) linker.<sup>55</sup>

Baimuratov et al. theoretically formulated exciton bands of two-dimensional super crystals with both hexagonal and centered rectangular lattices as well as square and rectangular lattices for the advancement of emerging nanophotonic technologies.<sup>52</sup> Their work was only on the formulation of exciton bands without experimental values. In our case, we predicted band structures of MOF using the theoretical equation in Bloch condition of Schrodinger equation combined with experimental parameters – optical absorption wavelength and material's dielectric constant. Thus, it is a unique method to predict the 1D array of any photonic nanocrystals' electronic band structures.

Additionally, MOFs have been tested as promising candidates for solar energy harvesting. Besides, a large proportion of the solar spectrum and most artificial light sources are in the visible spectrum. The progress of photocatalysts with high activity under visible-light irradiation is

required. Thus, new MOF materials with the visible light response are highly desirable.<sup>58</sup> Zhang et al. described exciton dynamics on MOF networks as a step-by-step random hopping. They monitored exciton migration by employing coumarin dye molecules in the MOF cavity as an emissive observer. They determined migration distances of exciton around 48 nm within their lifetimes.<sup>59</sup>

Most of the luminescence MOFs are based on lanthanide (having valence electron in 5d shell) containing MOFs.<sup>60-62</sup> Comparing that a smaller number of transition-metal-based luminescence MOFs have yet been found. Among the transition-metal-based luminescent MOFs, MOFs with Zn and Cd metal nodes are the most reported.<sup>63-65</sup> The research interest on IRMOFs for electronic properties, energy-harvesting, and photocatalysis applications is exploded by the recent studies on IRMOF-1 for photoluminescence<sup>66</sup> and solar energy harvesting and IRMOF-8 for optoelectronic properties.<sup>67</sup>

## ***2.4 Theoretical Background***

### **2.4.1 Analytical Approach to Predict Band Structure**

We can consider the 1D array of Zn MOF as a case of a valence electron in a solid. This electron may separate from its nucleus and travel through the material. An electron that travels through the crystal feels the entire crystal lattice's potential. A periodic delta-function potential can represent the stationary and evenly spaced lattice nuclei's influence.

Periodic potential in 1D space repeats itself after some fixed distance  $a$ . For the potential ( $V$ ) of a single particle,

$$V(x + a) = V(x)$$

Where  $a$  is the distance between two nodes and  $V(x)$  is the potential at the axis, and  $V(x+a)$  is the potential at distance ' $a$ '.

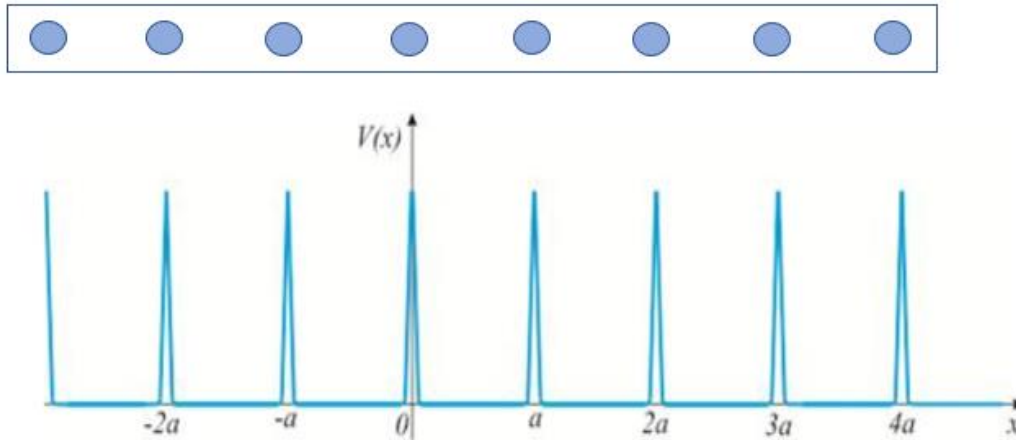


Figure 2: 1-D Array of Zn Metal Nodes and Corresponding Periodic Delta Function

Figure 2 is showing 1-D Array of Zn metal nodes and corresponding periodic delta function spike potential where blue dots are denoted Zn nodes

### 2.4.2 Implement of Bloch Theorem

The wave function of the particles has to be the solution of Schrödinger's equation

$$-\frac{\hbar^2}{2m} \frac{d^2}{dx^2} \psi(x) + V(x)\psi(x) = E\psi(x)$$

and has to satisfy Bloch's condition

$$\psi(x + a) = e^{ika}\psi(x)$$

or,

$$\psi(x) = e^{-ika}\psi(x + a)$$

where  $\Psi$  is the wavefunction,  $m$  is the mass of the electron,  $k$  is the wavenumber,  $\hbar$  is reduced Planck's constant, the wavenumber for the allowed zone,  $\kappa = \frac{2\pi n}{Na}$  and  $n = 0, \pm 1, \pm 2, \pm 3, \dots$

when we know  $\kappa$ , Bloch's theorem requires solving Schrödinger's equation just in one particular cell.<sup>68</sup> The recursive application of this equation generates solutions elsewhere. The set of delta function potentials can describe metal nodes of Zinc MOF:

$$V(x) = \alpha \sum_{j=0}^{N-1} \delta(x - ja)$$

Where  $\alpha$  is the amplitude of the potentials

Solution of Schrödinger's equation in region  $0 < x < a$ <sup>69,70</sup>:

$$\cos(\kappa a) = \cos(ka) + \frac{m\alpha}{\hbar^2 k} \sin(ka)$$

Let,  $f(z) = \cos(\kappa a)$ ,  $z = ka$ ,  $\beta = \frac{m\alpha a}{\hbar^2}$

Now,

$$\frac{m\alpha}{\hbar^2 k} = \frac{m\alpha a}{\hbar^2 ka} = \frac{\beta}{z}$$

So,

$$f(z) = \cos z + \beta \frac{\sin z}{z} \tag{1}$$

It is essential to realize that the value of the left-hand side varies between +1 to -1 as it is a cosine function  $\cos(\kappa a)$ , but the value of the right-hand side of the same equation can be higher or lower

than  $\pm 1$  due to the scaling factor next to the sinus. This equation can be solved only in the case when both sides match, and this represents the energy bands. If the right side is outside the range  $(-1,+1)$ , we cannot solve the equation describing the energy gap (or forbidden energies) between the bands.<sup>69,70</sup>

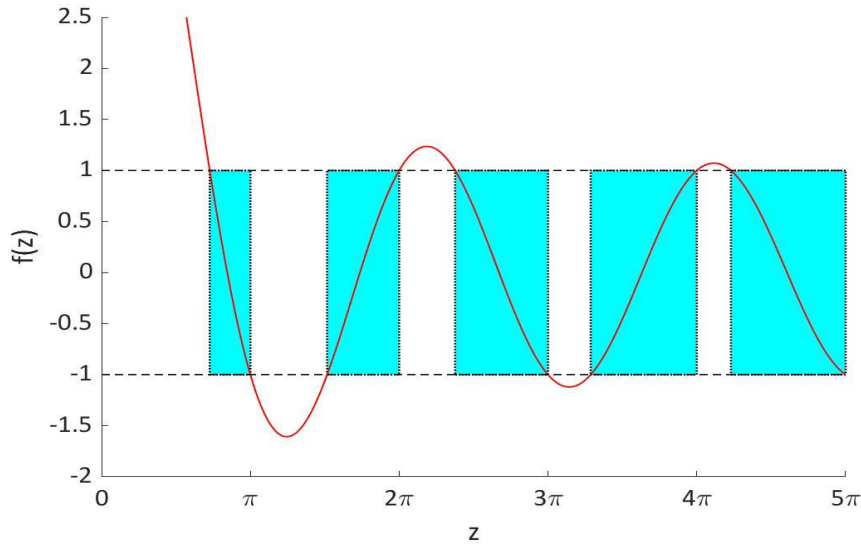


Figure 3: Graph of  $f(z)$  vs.  $z$  Showing Allowed Bands and Energy Gaps<sup>70</sup>

In energy band diagrams, energy bands' width depends on the absorption and emission energy. As absorption wavelength decreases, absorption energy and corresponding values of  $z$  and  $\beta$  also increase. It, in turn, shortens the width of the energy bands and broadens the width of band gaps. On the other hand, as emission wavelength decreases, emission energy and  $z$  value for absorption and the corresponding value of  $\beta$  also decreases. It, in turn, broadens the width of the energy bands and shortens the width of band gaps. Thus, the jump between the two allowed bands is reduced.

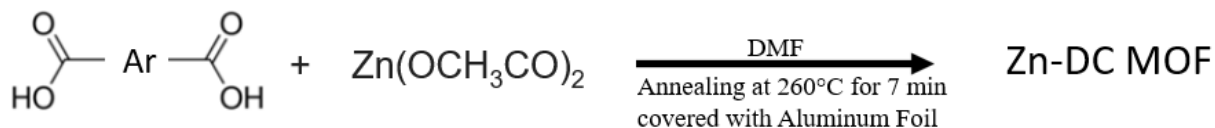


## CHAPTER III: EXPERIMENTAL PROCEDURES

### 3.1 Synthesis of Isorecticular Series of $Zn_4O(L)_3$ MOFs

IRMOF-1 (or MOF 5), IRMOF-8, and IRMOF-10 were synthesized by using Zinc acetate and Benzene- 1, 4- dicarboxylic acid (BDC), 2, 6- Naphthalene dicarboxylic acid (NDC), and Biphenyl- 4, 4'- dicarboxylic acid (BPDC), respectively.

#### 3.1.1 Reaction Scheme for the Synthesis Route of IRMOFs:



Where ‘Ar’ represents different types of aromatic rings and ‘DC’ is a short form of Dicarboxylic Acid

### 3.2 Synthesis Method

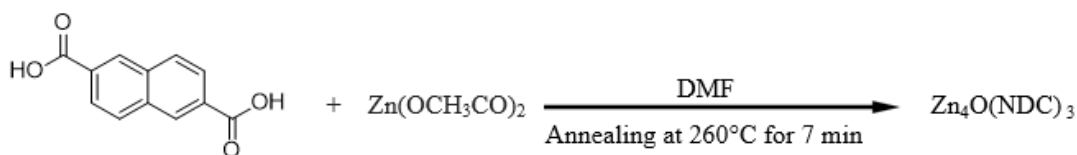
A rapid and self-assembly-driven solvothermal synthesis method was used. Three different microstructures of Isorecticular MOFs-nanocrystals were prepared from solutions of organic dicarboxylic acids (organic ligand) and metal precursors ( $\text{Zn}^{+2}$ ). Solvents are chosen according to the organic ligand and metal precursor’s solubility. In this case, dimethylformamide (DMF) is used as a solvent. Initially, the organic ligand and metal precursor are dissolved in a solvent using stirring at room temperature and then subjecting the reaction to solvothermal annealing at the temperature above the solvent’s boiling point for 7 minutes. After completing the reaction, the resulting off-white powders were collected to yield a pure crystalline product. The above reaction

summarizes the synthetic self-assembly path used to make microstructures of three different Isorecticular MOFs.<sup>67</sup>

### 3.2.1 Synthesis of IRMOF-8

Zn-NDC MOF (IRMOF-8) nanocrystals were prepared from solutions of 2,6-Naphthalene dicarboxylic acid (organic ligand) and metal precursor ( $\text{Zn}^{+2}$ ).

In a typical process, 2, 6- Naphthalene dicarboxylic acid (98.8 mg, 0.456 mmol) and zinc acetate (50 mg, 0.228 mmol) were added to anhydrous DMF (1 mL) solution in a crucible. The reactants were stirred for 10 minutes at room temperature. Then the crucible was covered by aluminum foil and heated to 260 °C for 7 minutes. After that, the sample was dried at room temperature for 12 hours. Finally, the resulting grayish powder was collected from both the crucible and the foil to yield the pure crystalline product for further characterization.

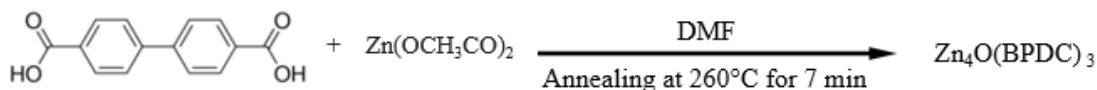


Reaction Scheme 1: The synthesis route to IRMOF-8 (Zn-NDC MOF)

### 3.2.2 Synthesis of IRMOF-10

At first, Long et al. introduced and synthesized Zn-BPDC MOF by hydrothermal reaction.<sup>71</sup> Zn-BPDC MOF (IRMOF-10) nanocrystals were prepared from solutions of Biphenyl- 4, 4'-dicarboxylic acid (organic ligand) and metal precursor ( $\text{Zn}^{+2}$ ).

In a typical process, Biphenyl- 4, 4'- dicarboxylic acid (110.5 mg, 0.456 mmol) and zinc acetate (50 mg, 0.228 mmol) were added to anhydrous DMF (1 mL) solution in a crucible. The reactants were stirred for 10 minutes at room temperature. Then the crucible was covered by aluminum foil and heated to 260 °C for 7 minutes. After that, the sample was dried at room temperature for 12 hours. Finally, the resulting grayish powder was collected from both the crucible and the foil to yield the pure crystalline product for further characterization.

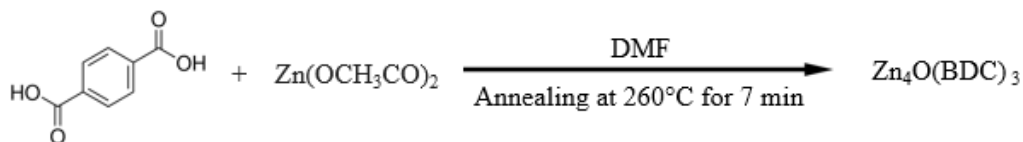


Reaction Scheme 2: The synthesis route to IRMOF-10 (Zn-BPDC MOF)

### 3.2.3 Synthesis of IRMOF-1

Zn-BDC MOF (MOF-5 or IRMOF-1) nanocrystals were prepared from solutions of Benzene- 1, 4- dicarboxylic acid (organic ligand), and metal precursor ( $\text{Zn}^{+2}$ ).

In a typical process, 1, 4 Benzene dicarboxylic acid (Terephthalic Acid) (75.8 mg, 0.456 mmol) and zinc acetate (50 mg, 0.228 mmol) were added to anhydrous DMF (1 mL) solution in a crucible. The reactants were stirred for 10 minutes at room temperature. Then the crucible was covered by aluminum foil and heated to 260 °C for 7 minutes. After that, the sample was dried at room temperature for 12 hours. Finally, the resulting grayish powder was collected from both the crucible and the foil to yield the pure crystalline product for further characterization.



Reaction Scheme 3: The synthesis route to IRMOF-1 (Zn-BDC MOF)

Different characterization of the synthesized three IRMOFs was performed, and properties were compared. The morphology studies, material composition, dielectric and photophysical properties of three different Isoreticular MOFs were analyzed.

### 3.3 Dielectric Properties

#### 3.3.1 Capacitor type Device Making

The ITO-coated glass substrate was ozone-treated by using Bio Force Ozone Pro Cleaner. Then it was cleaned by sonicating it in IPA for 15 mins followed by the sonication in DI water for 15 mins. After sonication, the substrate was dried with a nitrogen gun. Using a mask, 100 nm of copper as the first electrode was deposited on the cleaned and dried glass substrate by Physical Vapor Deposition (PVD) using the PVD 75 Evaporation System. Then 10 mg of Zn MOF in 500  $\mu\text{L}$  DMF and 500  $\mu\text{L}$  IPA were immediately spin-coated on the copper-deposited substrate at a spin rate of 3000 rpm for 60 seconds and dried for 12 hours. Then 100nm of copper as the second electrode was deposited again by PVD at a  $90^{\circ}$  rotation to the first layer by rotating the mask<sup>72</sup> (figure 10).

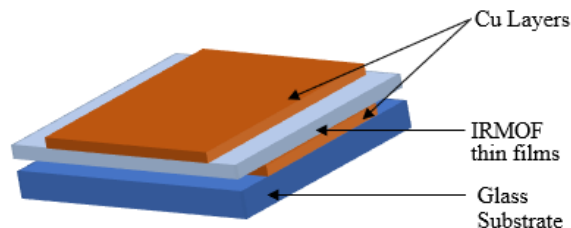


Figure 4: Schematic Diagram of Dielectric Capacitor

### **3.3.2 Capacitance Measurement**

Capacitance was then measured with a capacitometer (CM9610A) between the electrodes that form a capacitor area of  $4.75 \text{ cm}^2$ . Capacitance was measured in the 200 nF range.

### **3.3.3 Thickness Measurement**

The thin film's active layer thickness was measured by viewing a device's broken side under SEM. At first, the device was kept in liquid nitrogen for 5 minutes, and then it was broken to get the sharp edges. Finally, the sample was prepared for measuring the thickness. The broken side was rotated by  $60^\circ$ , and the tilt was corrected automatically by turning the tilt correction in SEM.

## ***3.4 Photophysical Properties***

### **3.4.1 UV-Vis Analysis**

IRMOF (1.0 mg) was added to anhydrous ethanol (1 mL) to make the UV-Vis analysis solution. For the baseline, ethanol was used in the cuvette. Then 250  $\mu\text{L}$  IRMOF solution was added to the cuvette with ethanol to check the absorption peak.

### **3.4.2 PL Analysis**

1 mg of MOF was added to 1mL solvent to make the solution for PL analysis. 250  $\mu\text{L}$  of MOF solution was added to the cuvette, filled with the PL analysis solvent to check the emission peak excited at a different wavelength. The range of wavelengths was taken to avoid excitation peaks and stokes shifts.

### 3.4.3 Solvent-Dependent Charge Transfer Dynamics Studies

To investigate the solvent-dependent charge transfer dynamics of IRMOFs in different polar solvents, the PL emission behavior of IRMOFs is explored in five different polar solvents by maintaining the same solute concentration in each solvent. Here we used Ethanol, Acetonitrile, Dimethylformamide (DMF), Tetrahydrofuran (THF), and Chloroform as polar solvents to dissolve three different IRMOFs as solute materials separately.

### 3.5 The Technique to Predict Band Structures

The solution of Schrödinger's equation in region  $0 < x < a$  in Bloch condition

$$f(z) = \cos z + \beta \frac{\sin z}{z} \quad (1)$$

Band structures were predicted from the absorbance and emission peak

#### 3.5.1 Considering only Metal Nodes

Necessary equations for absorption and emission energies were calculated from the wavelength for absorption and emission peak.

The wavelength for absorption peak =  $\lambda_{\text{absorption}}$  and wavelength for emission peak =  $\lambda_{\text{emission}}$

$$\text{The energy at emission peak, } E_{\text{emission}} = \frac{hc}{\lambda_{\text{emission}}}$$

$$\text{The energy at absorption peak, } E_{\text{absorption}} = \frac{hc}{\lambda_{\text{absorbance}}}$$

Where,  $hc = 1240 \text{ eVnm}$

If we know the wavelength of absorption and emission peak, we can calculate  $E_{\text{emission}}$  &  $E_{\text{absorption}}$ .

Since  $z = ka$  and  $\beta = \frac{m\alpha a}{\hbar^2}$ , we have  $\frac{\hbar^2}{ma} = \frac{\alpha}{\beta}$

$$\text{Energy, } E = \frac{\hbar^2 k^2}{2m} = \frac{\hbar^2 z^2}{2ma^2} = \left(\frac{z^2}{2a}\right) \left(\frac{\hbar^2}{ma}\right) = \left(\frac{z^2}{2a}\right) \left(\frac{\alpha}{\beta}\right)$$

To find  $z$  values, we can use  $E = \left(\frac{z^2}{2a}\right) \left(\frac{\alpha}{\beta}\right)$  for both energy values  $E_{\text{emission}}$  &  $E_{\text{absorption}}$

$$E_{\text{emission}} = \left(\frac{z_{\text{emission}}^2}{2a}\right) \left(\frac{\alpha}{\beta}\right) \quad (2)$$

$$E_{\text{absorption}} = \left(\frac{z_{\text{absorption}}^2}{2a}\right) \left(\frac{\alpha}{\beta}\right) \quad (3)$$

From equations 2 and 3, we find the relation between  $E$  &  $z$  for both absorption and emission.

$$\frac{E_{\text{absorption}}}{E_{\text{emission}}} = \left(\frac{z_{\text{absorption}}^2}{z_{\text{emission}}^2}\right) \quad (4)$$

The value of  $z$  for the emission peak,  $z_{\text{emission}}$  should be the maximum value of  $z$  for the first allowed energy band or the first bandgap's minimum value. The maximum value of  $k$  for the first allowed band is  $\frac{\pi}{a}$  and thus,  $z_{\text{emission}} = ka = \pi$ .

$$\frac{E_{\text{absorption}}}{E_{\text{emission}}} = \left(\frac{z_{\text{absorption}}^2}{\pi^2}\right)$$

From this equation, we can calculate the value of  $z$  for the absorption peak.

Finally, by plugging  $z$  in equation 1, we calculate the value of  $\beta$ . The range of the values for the left-hand side of equation 1,  $f(z)$  is from -1 to 1. For maximum, we have to plug either -1 or +1. But if we plug +1 for  $f(z)$ ,  $\beta$  is negative, but it is unrealistic as the amplitude of the potential cannot be negative. Thus, we have to plug -1 for  $f(z)$  to get a positive value for the amplitude of potential.

From equation 1 using the calculated  $\beta$  values, we can predict the energy band diagram for the 1D array of Zn-MOFs considering only metal nodes.<sup>73</sup>

### 3.5.2 Considering the Organic Ligands with Metal Nodes

The previous  $\beta$  value is hypothetical as we got this considering only metal nodes of Zn-MOFs. If we consider the organic parts and metal nodes, we have to bring dielectric constant in the picture. Considering the dielectric constant,  $\epsilon$ , we find a new value of  $\beta$  from the following equation:

$$\beta_{\text{new}} = \epsilon * \beta$$

From equation 1, using the calculated  $\beta_{\text{new}}$ , we can predict the energy band diagram for the 1D array of Zn-MOFs.

### 3.5.3 Calculations for Plotting Energy Curve

$$\cos(\kappa a) = \cos z + \beta \frac{\sin z}{z}$$

$$(\kappa a) = \left\{ \cos^{-1} \left( \cos z + \beta \frac{\sin z}{z} \right) \right\}$$

For allowed band Energy,  $E = \frac{(\kappa a)^2}{\pi^2}$



$$E = \frac{\hbar^2 \kappa^2}{2m} = \frac{\hbar^2 \kappa^2 a^2}{2ma^2} = \frac{\hbar^2 (\kappa a)^2}{2ma^2} = \frac{\hbar^2}{2ma^2} \left\{ \cos^{-1} \left( \cos z + \beta \frac{\sin z}{z} \right) \right\}^2$$

### 3.5.4 E vs $\kappa a$ for Showing Allowed Energy Bands

E vs  $\kappa a$  curves of Zn MOFs were plotted considering the organic part for different  $\beta_{\text{new}}$  values from MATLAB programming where the x-axis is  $\kappa a$ . Then E vs  $\kappa a$  curve was plotted for the 1-D array of different MOFs in a single plotting to compare the jumps between two allowed bands.

## CHAPTER IV: RESULTS AND DISCUSSION

### 4.1 Chemical Composition

#### 4.1.1 Functional Groups by FTIR

The chemical composition and functional groups of synthesized IRMOFs are analyzed using Fourier Transform Infrared Spectroscopy (FTIR-Varian 670-IR Spectrometer).

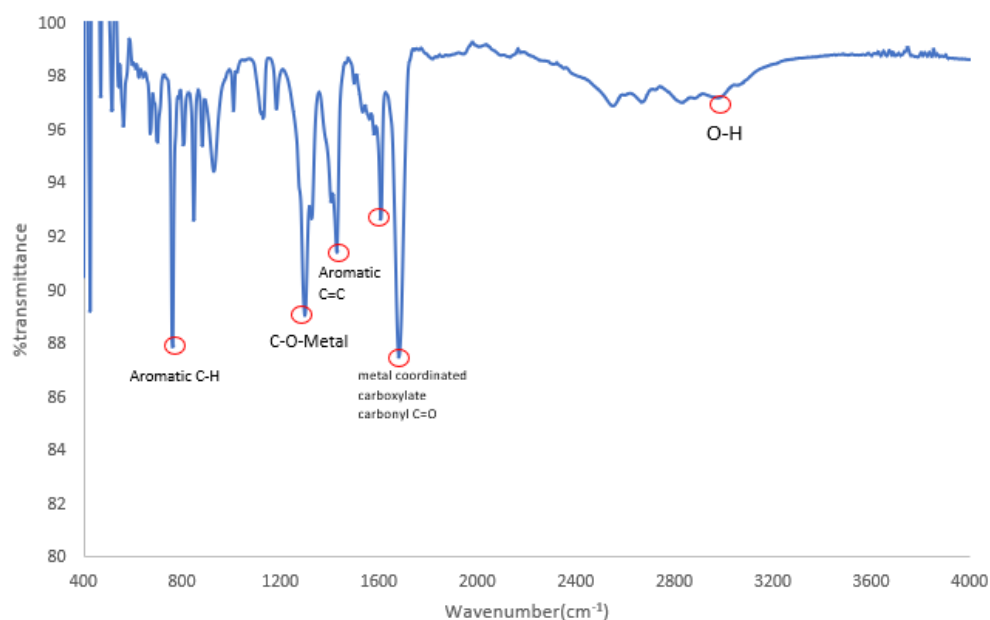


Figure 5: FTIR for IRMOF-1

Here, the FTIR spectrum (figure-5) of IRMOF-1 showed signals for metal coordinated carboxylate carbonyl stretching at  $1685\text{ cm}^{-1}$ , aromatic C=C bonds stretching at  $1540\text{--}1600\text{ cm}^{-1}$ , stretching from C-O-Zn at  $1400\text{--}1355\text{ cm}^{-1}$ , and broad O-H stretching at  $3158\text{ cm}^{-1}$ .

### 4.1.2 Chemical Composition, Oxidation States, and Chemical Environment by XPS

The chemical composition and purity, oxidation states, and nature of the chemical environments of different IRMOFs were confirmed from XPS.

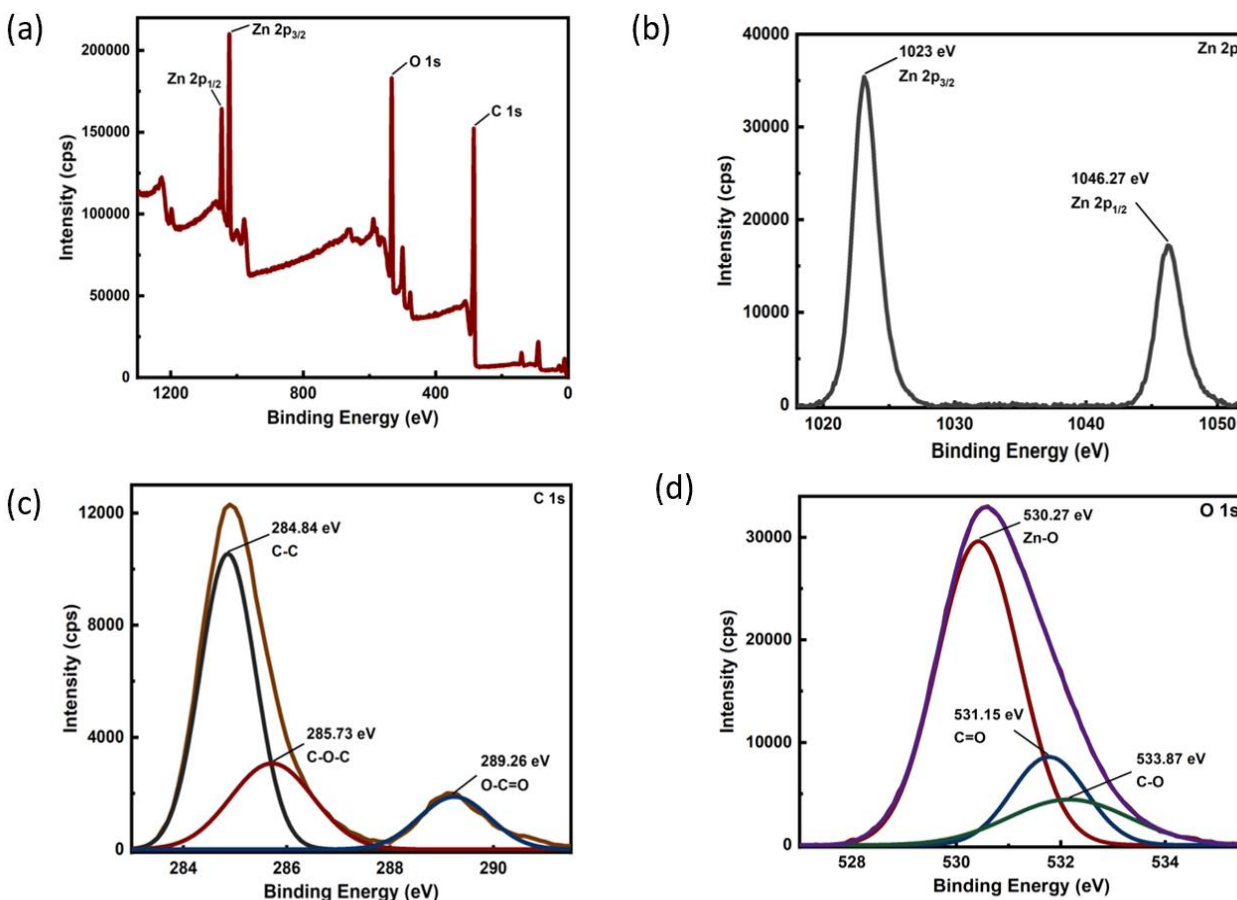


Figure 6: XPS of IRMOF-1: (a) XPS survey, (b) Zn 2p, (c) C 1s, and (d) O 1s

Figure 6 shows the X-ray photoelectron spectroscopy (XPS) survey spectrum and Zn 2p, C 1s, and O 1s binding energy spectra for IRMOF-1 (Zn-BDC MOF). The survey spectrum (Figure 6(a)) and resulted atomic % composition analysis confirmed the expected empirical formula of Zn-BDC MOF. The Zn 2p spectrum shown in Figure 6(b) revealed the oxidation state of zinc from the binding energy spectrum, which showed binding energies for the typical Zn<sup>+2</sup> oxidation state

concerning Zn 2p<sub>3/2</sub> and Zn 2p<sub>1/2</sub> spin-orbit states at 1021 eV and 1044.18 eV. C 1s spectrum shown in Figure 6(c) showed the deconvoluted three peaks attributing to three different chemical bonding environments, which belong to C–C, C–O–C, and O–C=O at 284.8, 285.15, and 288.86 eV, respectively. O 1s spectrum shown in Figure 6(d) showed the binding energy peak at 530.31 eV represents the Zn–C–O co-ordination bonds in IRMOF-1.

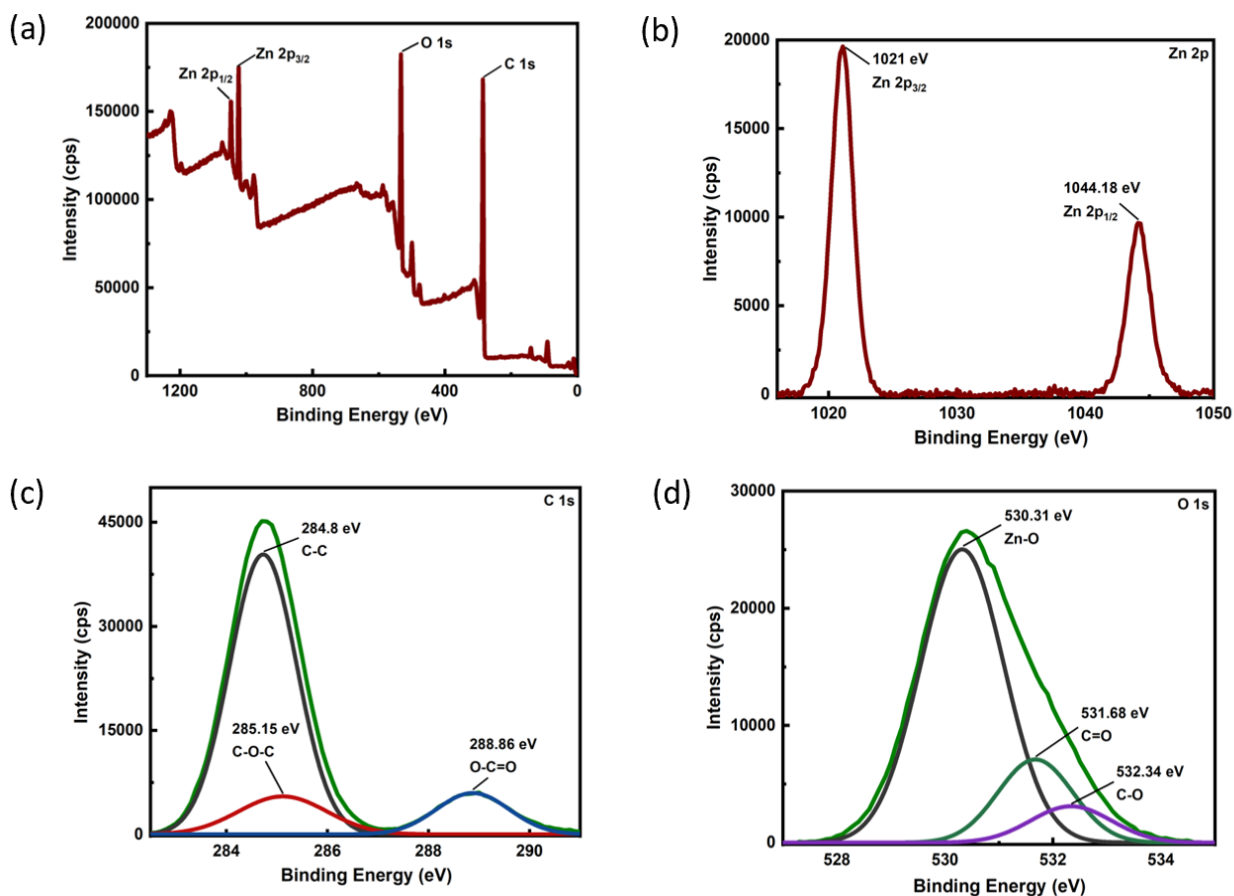


Figure 7: XPS of IRMOF-8: (a) XPS survey, (b) Zn 2p, (c) C 1s, and (d) O 1s

Figure 7 shows the X-ray photoelectron spectroscopy (XPS) survey spectrum and Zn 2p, C 1s, and O 1s binding energy spectra for IRMOF-8 (Zn-NDC MOF). The survey spectrum (Figure 7(a)) and resulted atomic % composition analysis confirmed the expected empirical formula of IRMOF-8. The Zn 2p spectrum shown in Figure 7(b) revealed the oxidation state of zinc from the binding

energy spectrum, which showed binding energies for the typical  $\text{Zn}^{+2}$  oxidation state concerning  $\text{Zn } 2p_{3/2}$  and  $\text{Zn } 2p_{1/2}$  spin-orbit states at 1021 eV and 1044.18 eV. C 1s spectrum shown in Figure 7(c) showed the deconvoluted three peaks attributing to three different chemical bonding environments, which belong to C-C, C-O-C, and O-C=O at 284.8, 285.15, and 288.86 eV, respectively. O 1s spectrum shown in Figure 7(d) showed the binding energy peak at 530.31 eV represents the Zn-C-O co-ordination bonds in IRMOF-8.

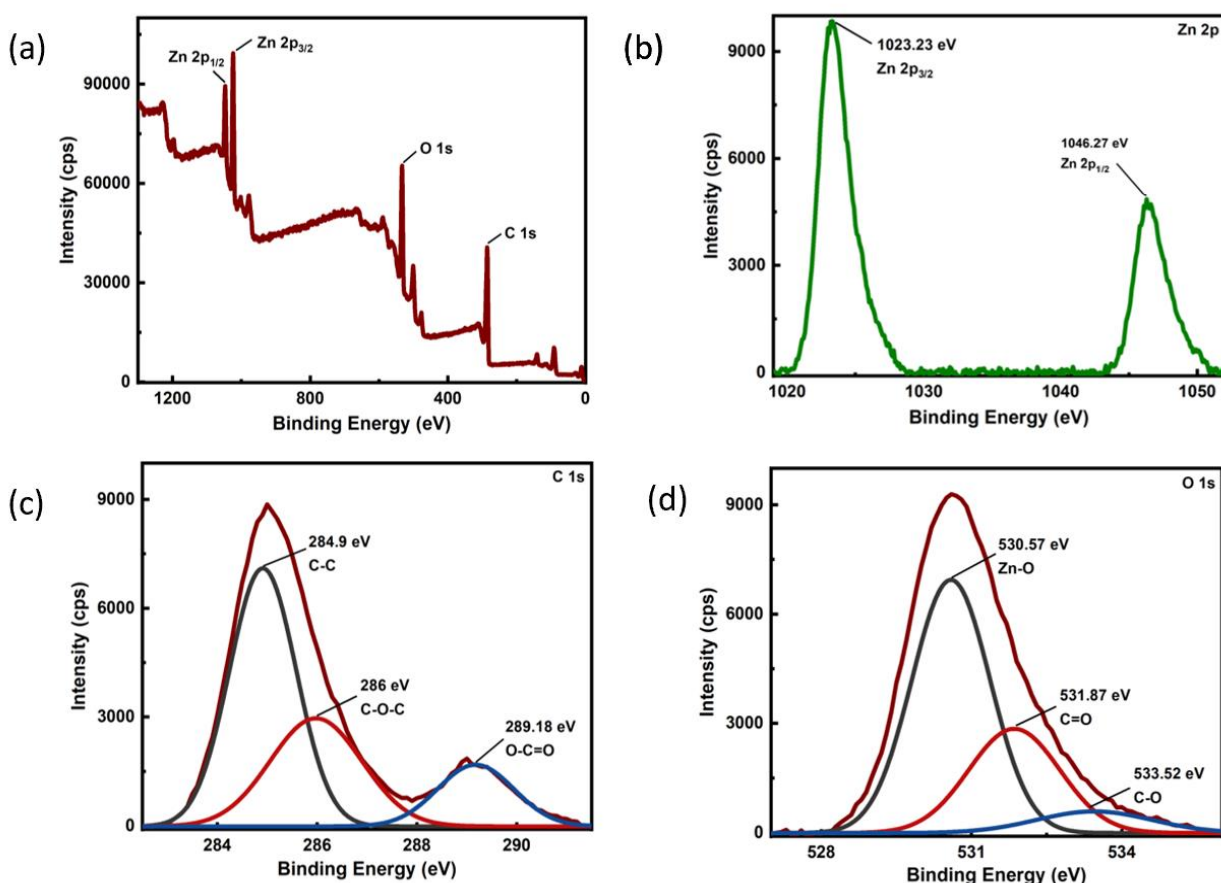


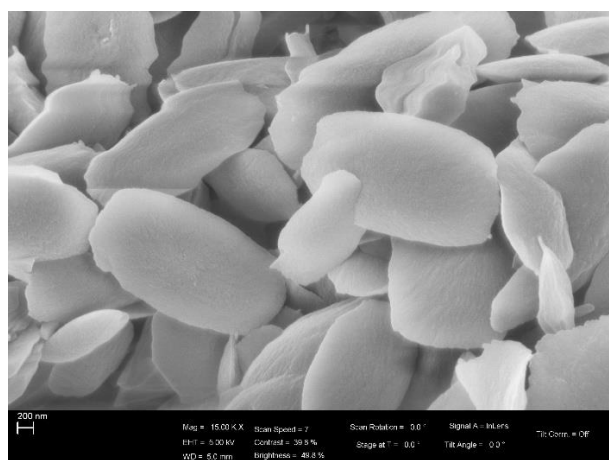
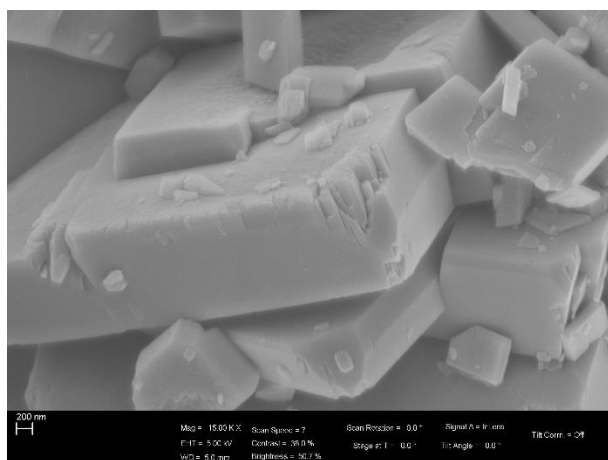
Figure 8: XPS of IRMOF-10: (a) XPS survey, (b) Zn 2p, (c) C 1s, and (d) O 1s

Figure 8 shows the X-ray photoelectron spectroscopy (XPS) survey spectrum along with Zn 2p, C 1s, and O 1s binding energy spectra for IRMOF-10 (Zn-BPDC MOF). The survey spectrum (Figure 8(a)) and resulted atomic % composition analysis confirmed the expected empirical

formula of IRMOF-10. The Zn 2p spectrum shown in Figure 8(b) revealed the oxidation state of zinc from the binding energy spectrum, which showed binding energies for the typical  $Zn^{+2}$  oxidation state concerning Zn 2p<sub>3/2</sub> and Zn 2p<sub>1/2</sub> spin-orbit states at 1023.23 eV and 1046.27 eV. C 1s spectrum shown in Figure 8(c) showed the deconvoluted three peaks attributing to three different chemical bonding environments, which belong to C–C, C–O–C, and O–C=O at 284.9 eV, 286 eV, and 289.18 eV, respectively. O 1s spectrum shown in Figure 8(d) showed the binding energy peak at 530.57 eV represents the Zn–C–O co-ordination bonds in IRMOF-10.

#### 4.2 Morphologies of IRMOFs

The morphology of IRMOF microstructures was analyzed using scanning electron microscopy (Zeiss Auriga FIB/FESEM).



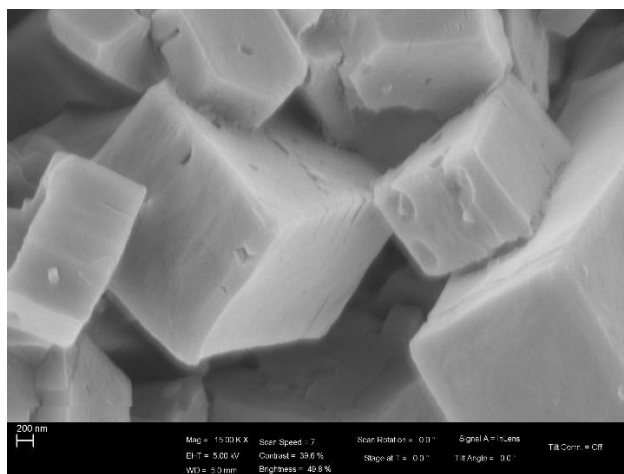


Figure 9: SEM of IRMOF-8 (top left), IRMOF-10 (top right), and IRMOF-1(bottom)

Microstructures of IRMOF-8 (Figure 9) show Cuboid-type structures. IRMOF-10 and IRMOF-1 have ellipse and cubic-type structures, respectively.

#### ***4.3 Structural Properties by XRD***

The crystal structures of IRMOFs were confirmed by the experimental powder X-ray Diffraction (XRD) analysis combined with the simulated XRD spectra obtained for the original crystal structures of IRMOF-1, IRMOF-8, and IRMOF-10 from the Cambridge Crystallographic Data Center (IRMOF-1: Deposition no. CCDC-256965, IRMOF-8: Deposition No. CCDC-957268, IRMOF-10: Deposition No. CCDC-190973) and the cif files of IRMOF-1, IRMOF-8 and IRMOF-10<sup>74-76</sup>. Simulated powder XRD spectra of IRMOFs were generated from VESTA by selecting the “Powder diffraction pattern” function from “Utilities”.

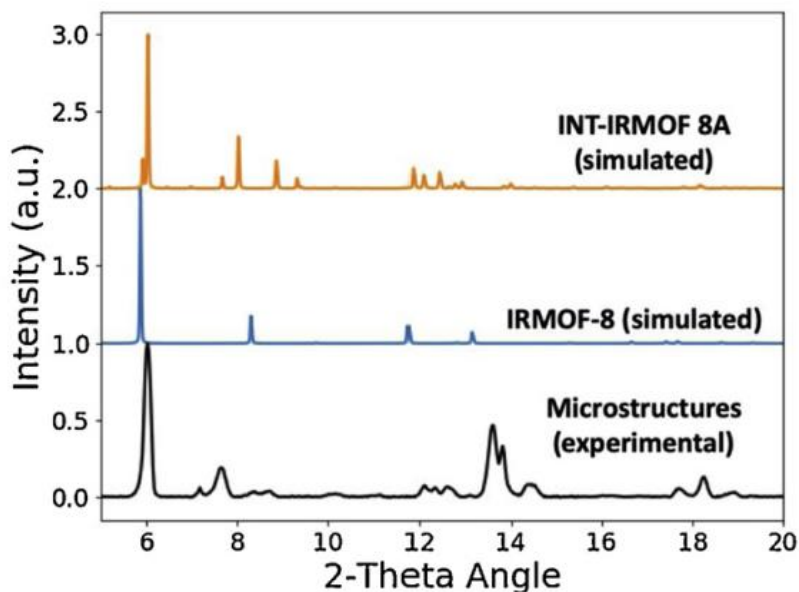


Figure 10: XRD Spectrum of IRMOF-8 (Experimental and Simulated)<sup>77</sup>

The experimental XRD pattern of IRMOF-8 microstructures was compared with the simulated powder XRD spectra of IRMOF-8, and INT-IRMOF-8 A, generated from the crystal structures of IRMOF-8 and INT-IRMOF-8 A, deposited in the crystallographic data bank (Deposition No. CCDC-957268), and are represented in Figure 10. The experimental diffraction pattern of synthesized IRMOF-8 overlaps with the simulated XRD spectral pattern of INT-IRMOF-8 A, which confirms the similarity of generated unit cell crystal structure of the microstructures from the powder XRD pattern is similar to the reported crystal structure of the INT- IRMOF-8A.<sup>78</sup>



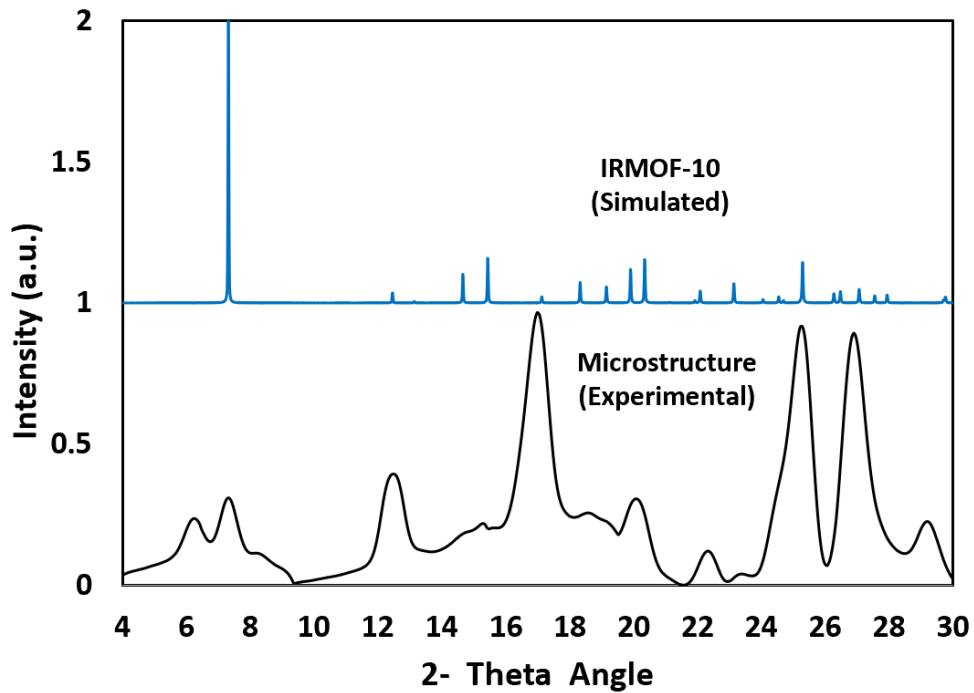


Figure 11: XRD Spectrum of IRMOF-10 (Experimental and Simulated)

The experimental XRD pattern of IRMOF-10 microstructures was compared with the simulated powder XRD spectra of IRMOF-10, generated from the crystal structures of IRMOF-10, deposited in the crystallographic data bank (Deposition No. CCDC-190973), and are represented in Figure 11. The experimental diffraction pattern of synthesized IRMOF-10 overlaps with the simulated XRD spectral pattern of IRMOF-10.

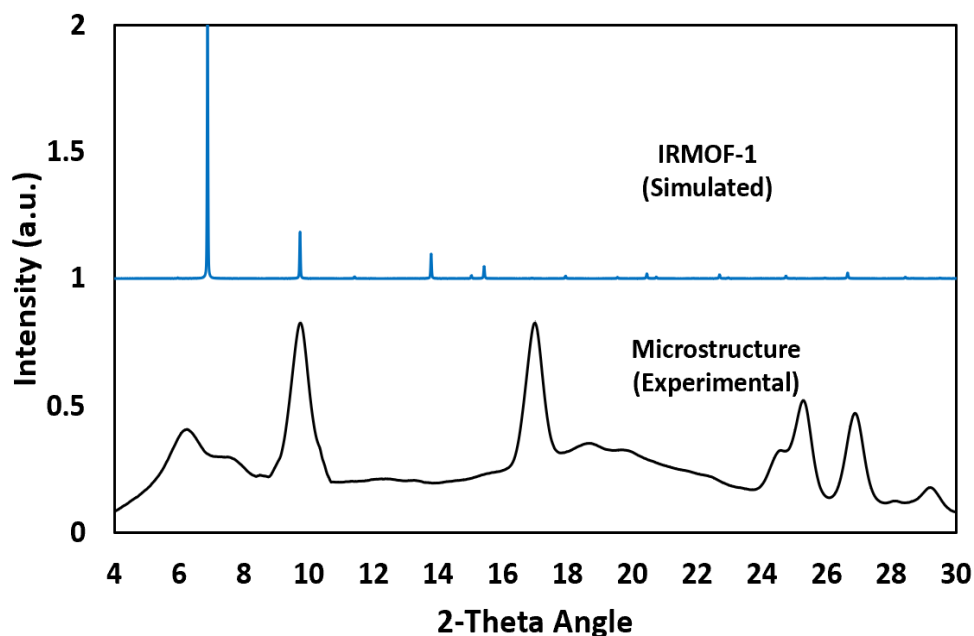


Figure 12: XRD Spectrum of IRMOF-1 (Experimental and Simulated)

The experimental XRD pattern of IRMOF-1 microstructures was compared with the simulated powder XRD spectra of IRMOF-1, generated from the crystal structures of IRMOF-1, deposited in the crystallographic data bank (Deposition No. CCDC-256965), and are represented in Figure 12. The experimental diffraction pattern of synthesized IRMOF-1 overlaps with the simulated XRD spectral pattern of IRMOF-1.

#### ***4.4 Photophysical Properties***

##### **4.4.1 Absorption and Emission Spectra for Band Structure**

Absorption and emission energy were calculated from absorption and emission spectra maxima.

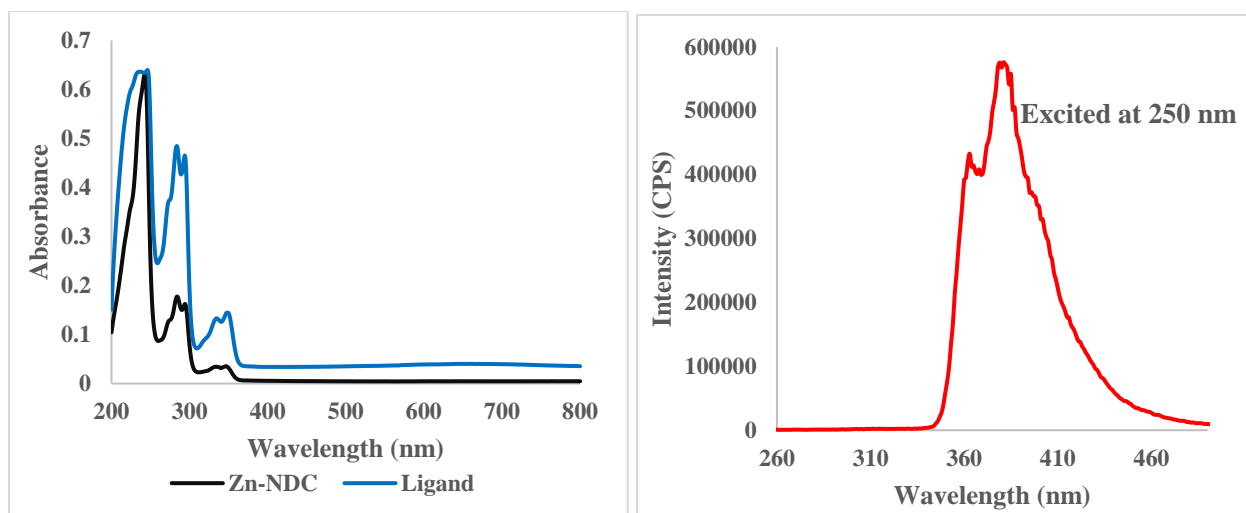


Figure 13: UV-Vis (left) & PL-Analysis (right) for IRMOF-8

For IRMOF-8, the absorbance peak was found at 243nm. After excited at 250nm, the emission peak was 385nm.

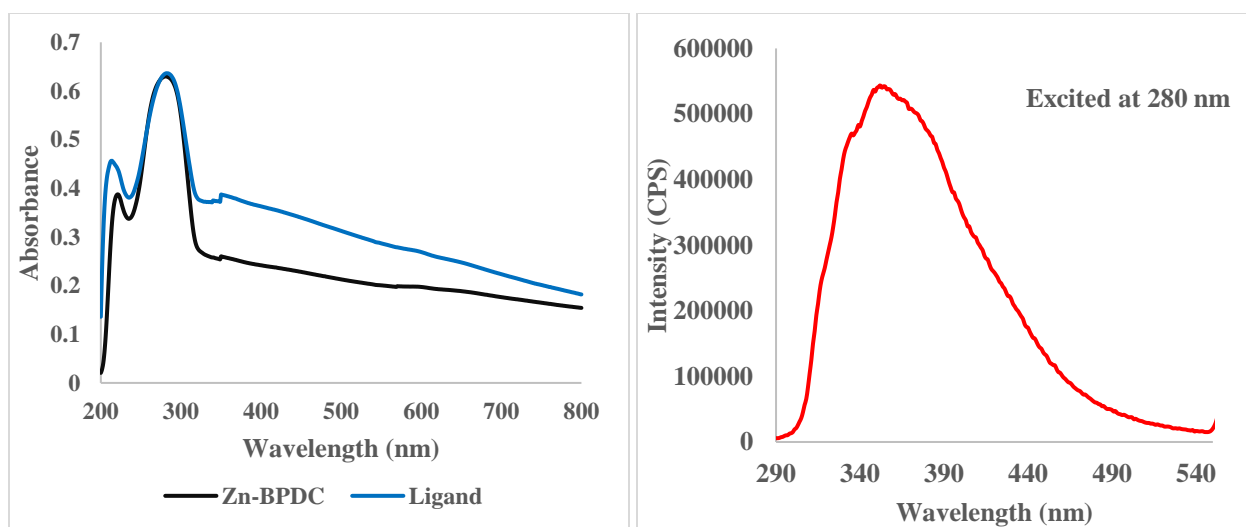


Figure 14: UV-Vis (left) & PL-Analysis (right) for IRMOF-10

For IRMOF-10, the absorbance peak was found at 281nm. After excited at 280nm, the emission peak was 352nm.

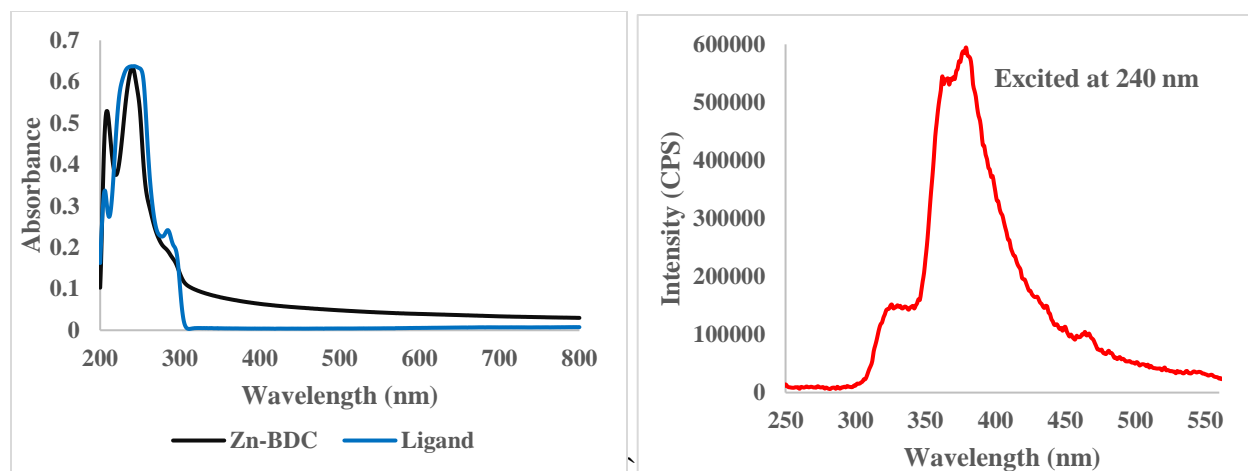


Figure 15: UV-Vis (left) & PL-Analysis (right) for IRMOF-1

For IRMOF-1, the absorbance peak was found at 240nm. After excited at 240nm, the emission peak was 379 nm.

The longer the conjugation length, the lower the separation between adjacent energy levels. The longer the absorption wavelength as the absorption band in the visible region is increasingly red-shifted, the conjugation length increases. Hence, with larger conjugated systems, the absorption peak wavelengths tend to be shifted toward the long-wavelength region. BPDC linker has a longer conjugation length than NDC and BDC linkers. Thus, the absorption peaks for IRMOF-10 moved toward the longer wavelength region than the other two MOFs.

#### 4.4.2 Solvent-Dependent Photoluminescence Emission

We performed PL analysis of different IRMOFs in five different polar solvents. We used Ethanol, Acetonitrile, Dimethylformamide (DMF), Tetrahydrofuran (THF), and Chloroform to dissolve IRMOFs. We collected PL data with the same amount of each solute (IRMOF) concentration in different solvents. Photoluminescence Emission Spectra of three IRMOFs were analyzed separately with emission intensity comparison in those five solvents. We observed the impact of

the solvent type on the intensity of fluorescence emission during our solvent-dependent fluorescence studies.

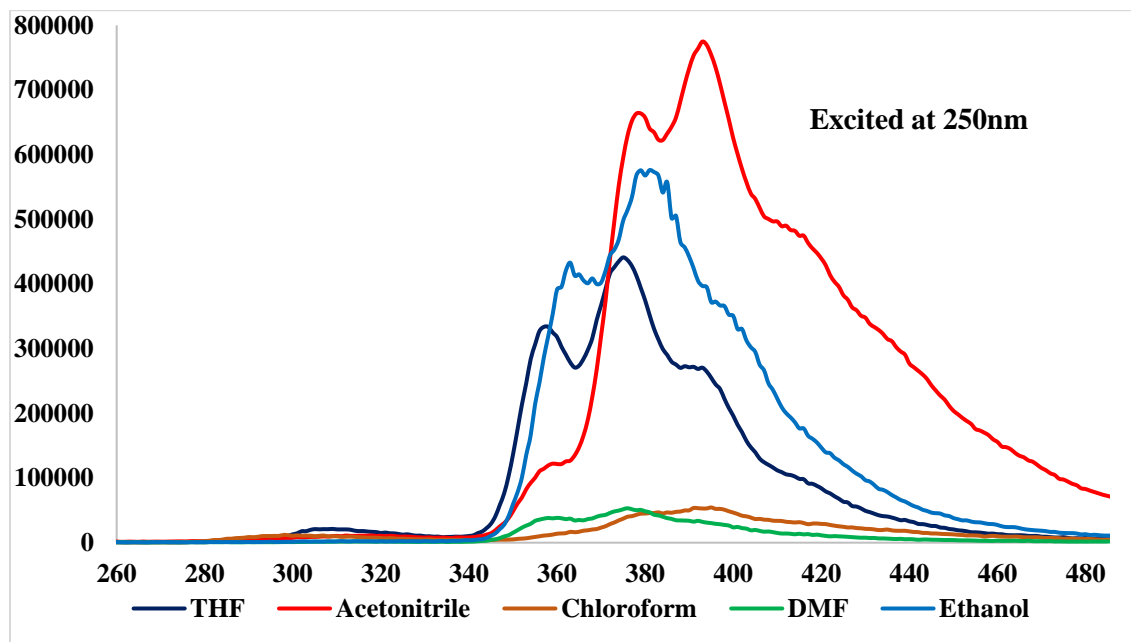


Figure 16: PL Emission Spectra of IRMOF-8 in Five Different Polar Solvents

In Figure 16, PL emission intensity of IRMOF-8 is compared in five different polar solvents maintaining the same solute concentration. Here, ligand-centered emission is observed for IRMOF-8 in THF solvent, apart from 5 nm and 6 nm blue-shifted PL emission peak maxima compared to the emission vibronic peak maxima at 363 and 381 nm in ethanol. The photoluminescence emission intensity of IRMOF-8 in THF exhibits about 22% decrease compared to the photoluminescence emission intensity in ethanol, having the same solute concentration. There is no evidence of solvent-dependent charge transfer transition occurred for IRMOF-8 in THF as in ethanol. The PL intensity of IRMOF-8 in acetonitrile exhibits 33% increase compared to the intensity of IRMOF-8 in ethanol. However, we observed significant quenching of the PL intensity of IRMOF-8 in DMF and chloroform. The ligand-centered emission of IRMOF-8 is wholly quenched in both solvents DMF and chloroform. In DMF, the emission peak is not

much shifted from the peak in THF or ethanol, but in chloroform and acetonitrile, the emission peak in PL spectra is found at the longer wavelength, 395 nm. This longer wavelength emission band in chloroform and acetonitrile may be attributed to ligand-to-metal charge transfers (LMCT) transition.

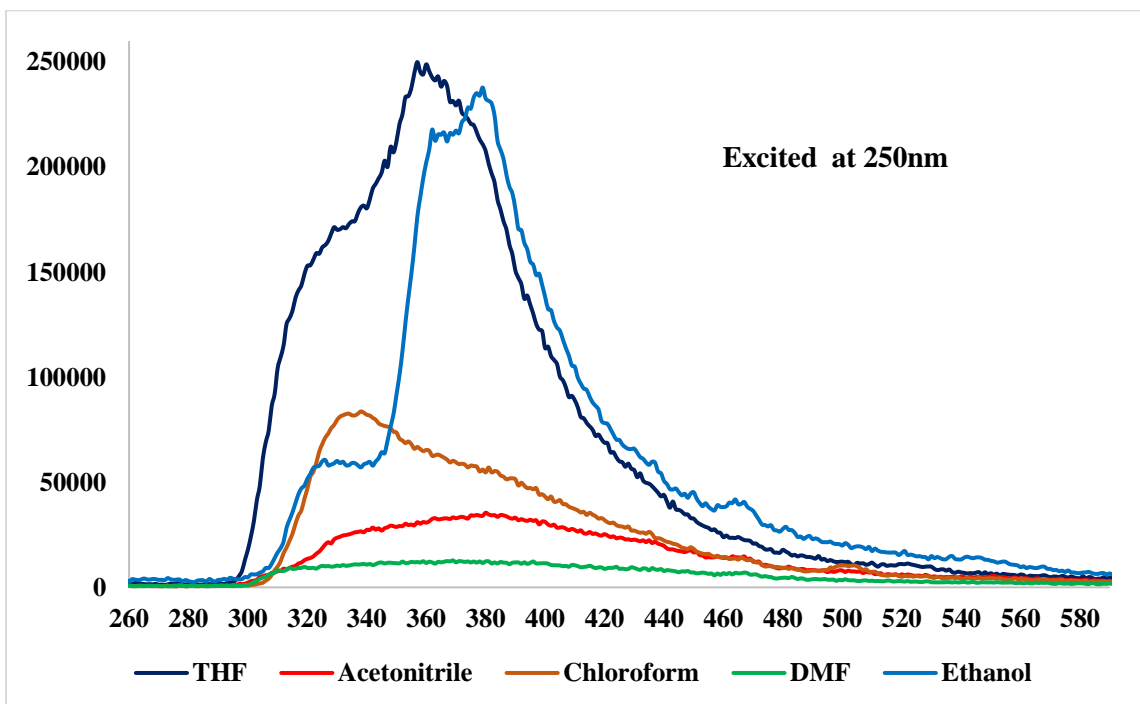


Figure 17: PL Emission Spectra of IRMOF-1 in Five Different Polar Solvents

In Figure 17, PL emission intensity of IRMOF-1 is compared in five different polar solvents maintaining the same solute concentration. Here, ligand-centered emission is observed for IRMOF-1 in THF solvent, apart from 12 nm blue-shifted PL emission peak maxima compared to the emission vibronic peak maxima at 377 nm in ethanol. The photoluminescence emission intensity of IRMOF-1 in THF exhibits about 6% increase compared to the photoluminescence emission intensity in ethanol, having the same solute concentration. There is no evidence of solvent-dependent charge transfer transition occurred for IRMOF-1 in THF as in ethanol. However, we observed significant quenching of the PL intensity of IRMOF-1 in acetonitrile, DMF,

and chloroform. The ligand-centered emission of IRMOF-1 is wholly quenched in three solvents- acetonitrile, DMF, and chloroform. In DMF and acetonitrile, the emission peak is not much shifted from the peak in THF or ethanol. Still, in chloroform, the emission peak in PL spectra is found at the shorter wavelength, 340 nm, attributed to the LMCT transition.

The longer wavelength emission band in chloroform and acetonitrile may be attributed to ligand-to-metal charge transfers (LMCT) transition, which is induced by dipole-dipole interactions of solvent and solute, creating local electrostatics and could control the electron density distribution around the IRMOF framework.<sup>25</sup> The reshaping of the electron density distribution between the metal ion node and the organic ligand and dispersing the solute in different polar solvents may facilitate the energy transfer from the ligand to the metal node via LMCT transition.<sup>79,80</sup>

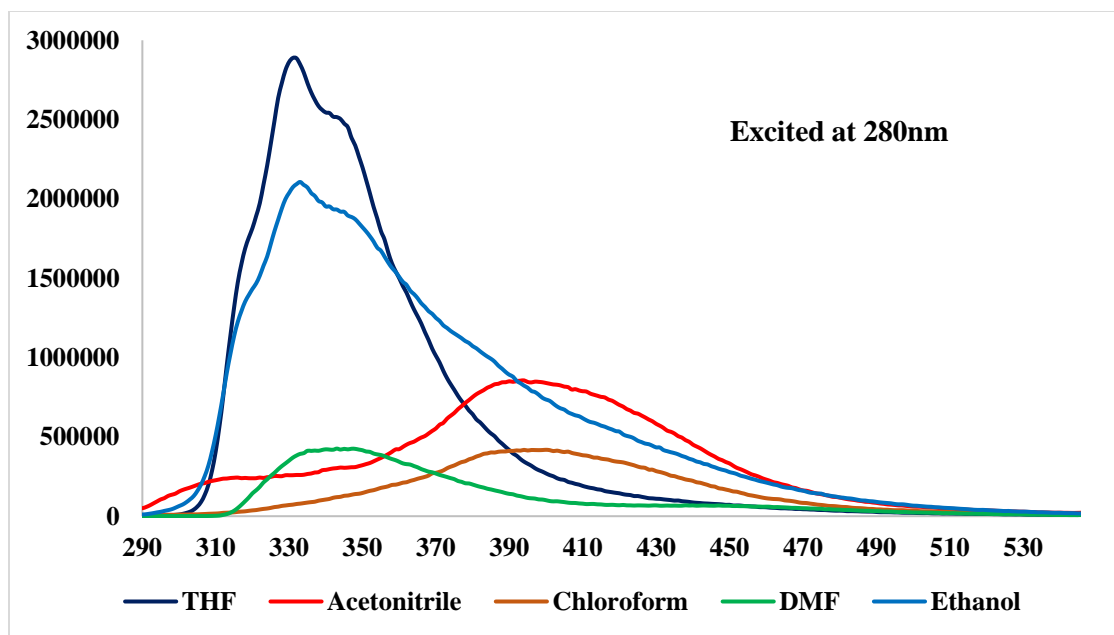


Figure 18: PL Emission Spectra of IRMOF-10 in Five Different Polar Solvents

In Figure 16, PL emission intensity of IRMOF-10 is compared in five different polar solvents maintaining the same solute concentration. Here, ligand-centered emission is observed for

IRMOF-10 in THF solvent, apart from 2 nm blue-shifted PL emission peak maxima in compared to the emission vibronic peak maxima at 334 nm in ethanol. The photoluminescence emission intensity of IRMOF-10 in THF exhibits about 37% increase compared to the photoluminescence emission intensity in ethanol, having the same solute concentration. There is no evidence of solvent-dependent charge transfer transition occurred for IRMOF-10 in THF as in ethanol. However, we observed significant quenching of the PL intensity of IRMOF-10 in acetonitrile, DMF, and chloroform. The ligand-centered emission of IRMOF-10 is wholly quenched in three solvents- acetonitrile, DMF, and chloroform. In DMF, the emission peak is not much shifted from the peak in THF or ethanol. Still, in chloroform and acetonitrile, the emission peak in PL spectra is found at the longer wavelength, 397 nm, attributed to the LMCT transition.

#### ***4.5 Thermal Stability***

The thermal stability of IRMOFs was found from the Thermogravimetric Analysis (TGA). We got the idea of the temperature zone from the analysis where the removal of phenyl rings and carboxylate groups from organic ligands occurred. The TGA analysis shows the temperature up to which synthesized IRMOFs are stable, and beyond this temperature, the decomposition and collapsing of the framework occur.



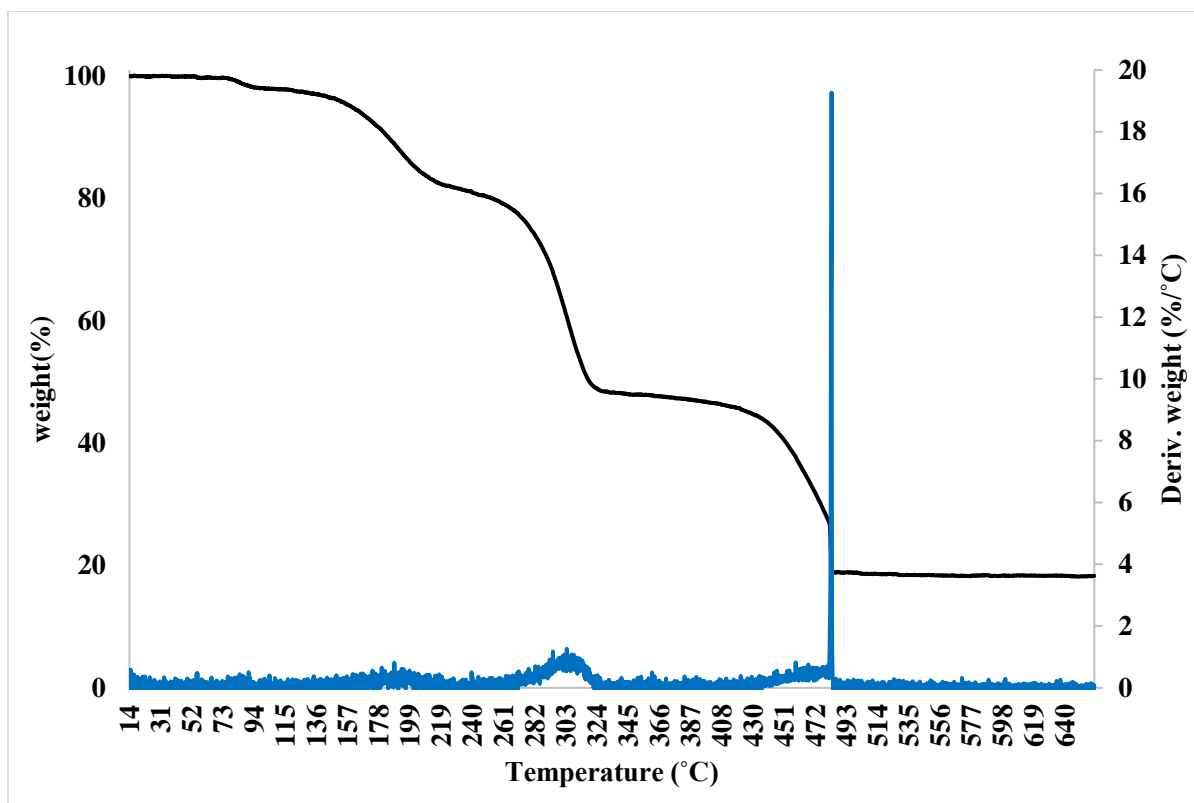


Figure 19: TGA for IRMOF-1

TGA of IRMOF-1 shows three distinct weight losses at 190 °C, 305 °C, and 440 to 480 °C. The initial weight loss of less than 15% at 190 °C was due to the loss of free and lattice water molecules and solvent molecules (DMF) incorporated into the microstructure’s void spaces. The second weight loss of 40% can be attributed to removing carboxylate groups and phenyl rings from organic ligands. The temperature range of 440–480 °C is showing the indication of decomposing the residual organic fractions (30% weight loss) and collapsing the framework to form the residual metal oxide. The TGA analysis verified that microstructures of IRMOF-1 are thermally stable up to 305 °C.

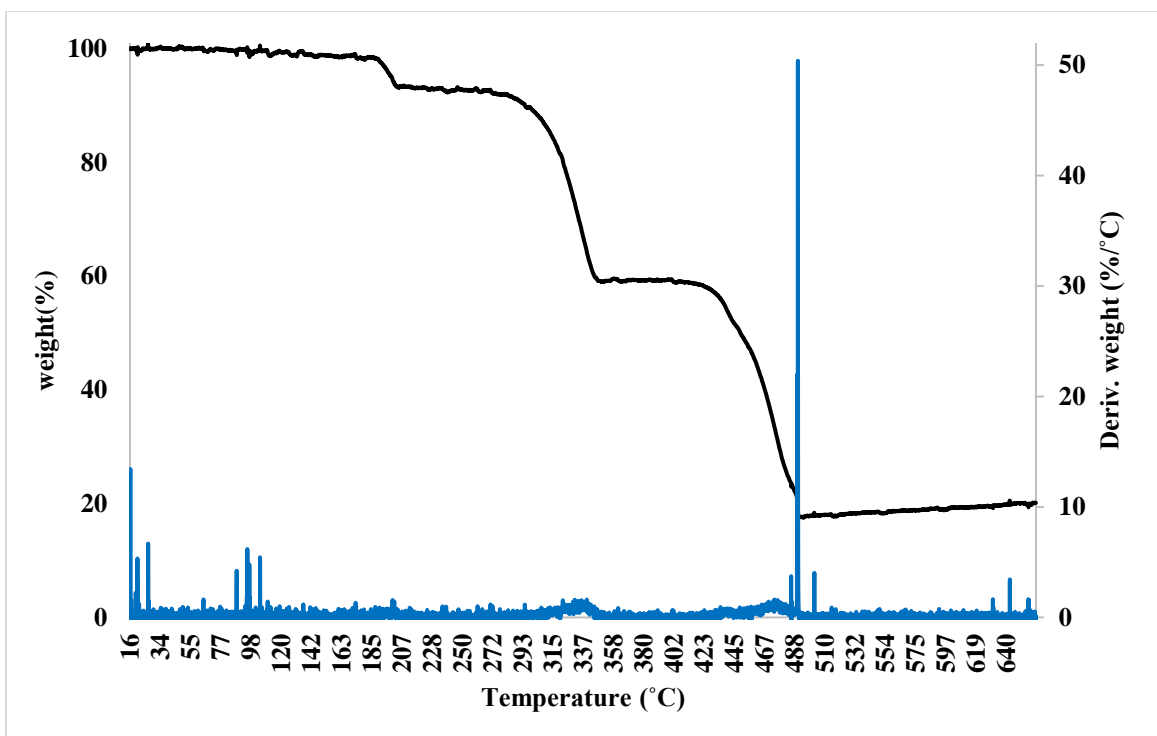


Figure 20: TGA for IRMOF-8

TGA for IRMOF-8 shows three distinct weight losses at 200 °C, 340 °C, and 440 to 490 °C. The initial weight loss of less than 10% at 200 °C could be due to the loss of free and lattice water molecules and solvent molecules (DMF) incorporated into the microstructure’s void spaces. The second weight loss of 40% can be attributed to removing carboxylate groups and phenyl rings from organic ligands. The temperature range of 440–500 °C is showing the indication of decomposing residual organic fractions (40% weight loss) and collapsing the framework to form the residual metal oxide. The TGA analysis verified that IRMOF-8 microstructures are thermally stable up to 340 °C.

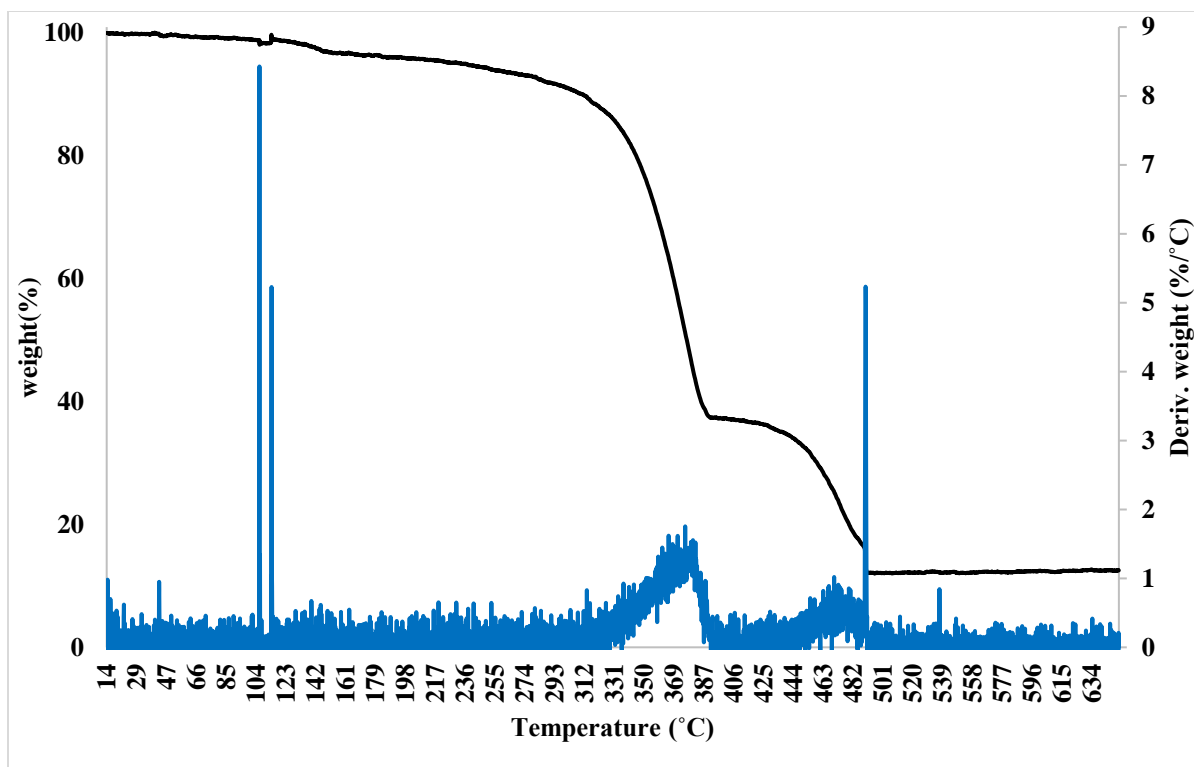


Figure 21: TGA for IRMOF-10

TGA for IRMOF-10 shows three distinct weight losses at 210 °C, 360 °C, and 450 to 490 °C. The initial weight loss of less than 10% at 260 °C could be due to the loss of free and lattice water molecules and solvent molecules (DMF) incorporated into the microstructure’s void spaces. The second weight loss of 55% can be attributed to removing carboxylate groups and phenyl rings from organic ligands. The temperature range of 450–490 °C is showing the indication of decomposing residual organic fractions (30% weight loss) and collapsing the framework to form the residual metal oxide. The TGA analysis verified that microstructures of IRMOF-10 are thermally stable up to 360 °C.

## 4.6 Dielectric Properties

The dielectric constant depends on ligand size. The longer the ligand size for IRMOFs, the higher the dielectric constant of IRMOFs.

### 4.6.1 Thin-Film Thickness Measurement from SEM

Thin-film thickness was found from the SEM image (Figure 22) of the cross-sectional part of the capacitor type device.

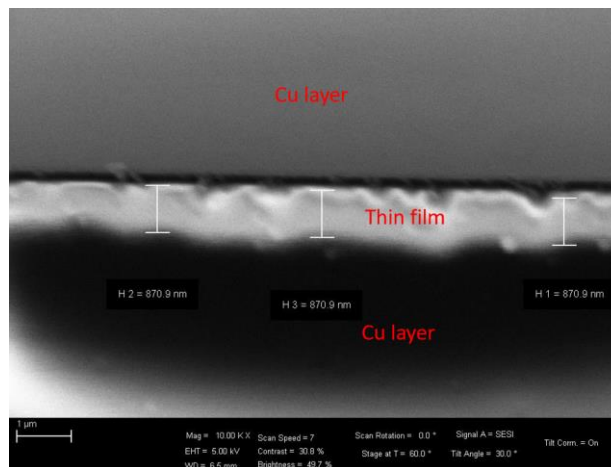


Figure 22: SEM Image of the Cross-Sectional Part of the Device

### 4.6.2 Dielectric Constant Calculation

The dielectric constant was measured from the formulae,

$$\varepsilon = \frac{tC_p}{SK_0}$$

Where  $\varepsilon$  is the dielectric constant,  $t$  is the thickness of thin-film,  $C_p$  is the capacitance of the device, and  $S$  is the capacitor zone's surface area.

Capacitance was measured in nF by the capacitometer (CM9610A).

Table 1: Dielectric Constant Calculation from Capacitance for IRMOF-8

<b>C<sub>p</sub>(nF)</b>	<b>S(m<sup>2</sup>)</b>	<b>K<sub>o</sub>(F/m)</b>	<b>t(nm)</b>	<b>ε</b>
14.3	0.000475	8.85E-12	870.9	2.96
14.2	0.000475	8.85E-12	870.9	2.94
13.9	0.000475	8.85E-12	870.9	2.88
14.0	0.000475	8.85E-12	870.9	2.90
14.2	0.000475	8.85E-12	870.9	2.94
14.3	0.000475	8.85E-12	870.9	2.96
13.8	0.000475	8.85E-12	870.9	2.86
14.1	0.000475	8.85E-12	870.9	2.92
14.0	0.000475	8.85E-12	870.9	2.90

Table 2: Dielectric Constant Calculation from Capacitance for IRMOF-10

<b>C<sub>p</sub>(nF)</b>	<b>S(m<sup>2</sup>)</b>	<b>K<sub>o</sub>(F/m)</b>	<b>t(nm)</b>	<b>ε</b>
13.8	0.000475	8.85E-12	769.3	2.53
13.9	0.000475	8.85E-12	769.3	2.54
13.7	0.000475	8.85E-12	769.3	2.51
14.0	0.000475	8.85E-12	769.3	2.56
13.6	0.000475	8.85E-12	769.3	2.49
13.7	0.000475	8.85E-12	769.3	2.51
13.8	0.000475	8.85E-12	769.3	2.53
14.1	0.000475	8.85E-12	769.3	2.58
13.8	0.000475	8.85E-12	769.3	2.53

Table 3: Dielectric Constant Calculation from Capacitance for IRMOF-1

$C_p(\text{nF})$	$S(\text{m}^2)$	$K_o(\text{F/m})$	$t(\text{nm})$	$\epsilon$
13.4	0.000475	8.85E-12	770	2.45
13.5	0.000475	8.85E-12	770	2.47
13.7	0.000475	8.85E-12	770	2.51
13.6	0.000475	8.85E-12	770	2.49
13.4	0.000475	8.85E-12	770	2.45
13.3	0.000475	8.85E-12	770	2.44
13.5	0.000475	8.85E-12	770	2.47
13.7	0.000475	8.85E-12	770	2.51
13.6	0.000475	8.85E-12	770	2.49

Standard deviations of the values of the dielectric constant of three IRMOFs are less than 0.04

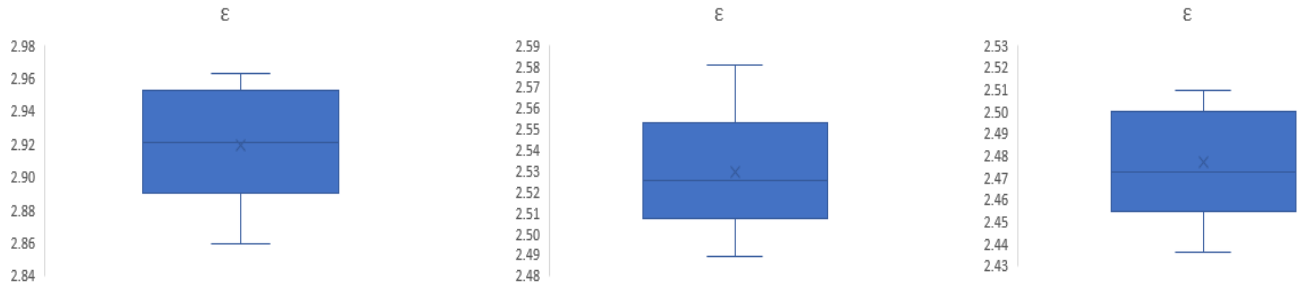


Figure 23: Comparing  $\epsilon$  Values (from left to right: IRMOF-8, IRMOF-10, IRMOF-1)

The dielectric constant depends on ligand length but not on the ligand's conjugation length. The longer the ligand length of organic linkers, the higher the value of dielectric constant for corresponding MOFs. The ligand length of the NDC linker is more than BPDC, and BDC linker as benzene rings of BPDC is perpendicular, and the BDC linker has the lowest ligand length. Thus, the dielectric constant is decreasing from IRMOF-8 (2.919) to IRMOF-10 (2.529) and IRMOF-1 (2.477).

#### 4.7 $\beta$ Calculation Considering Only Metal Nodes

The solution of Schrödinger's equation in region  $0 < x < a$  in Bloch condition

$$f(z) = \cos z + \beta \frac{\sin z}{z} \quad (1)$$

Necessary equations for absorption and emission energies:

$$E_{\text{emission}} = \left( \frac{z_{\text{emission}}^2}{2a} \right) \left( \frac{\alpha}{\beta} \right) \quad (2)$$

$$E_{\text{absorption}} = \left( \frac{z_{\text{absorption}}^2}{2a} \right) \left( \frac{\alpha}{\beta} \right) \quad (3)$$

Band structures of MOFs are predicted from the dielectric constant, the wavelength of absorbance, and emission peak.

##### 4.7.1 $\beta$ for IRMOF-8 (Zn-NDC MOF)

For Zn-NDC MOF,  $\lambda_{\text{absorption}} = 243 \text{ nm}$  and  $\lambda_{\text{emission}} = 385 \text{ nm}$ ,

$$E_{\text{emission}} = \frac{hc}{\lambda_{\text{emission}}} = \frac{1240 \text{ eVnm}}{385 \text{ nm}} = 3.221 \text{ eV}$$

$$E_{\text{absorption}} = \frac{hc}{\lambda_{\text{absorption}}} = \frac{1240 \text{ eVnm}}{243 \text{ nm}} = 5.103 \text{ eV}$$

From equation 2 and 3:

For  $E_{emission}$ .

$$3.221 = \left(\frac{\pi^2}{2a}\right)\left(\frac{\alpha}{\beta}\right)$$

For  $E_{absorption}$ .

$$5.103 = \left(\frac{z^2}{2a}\right)\left(\frac{\alpha}{\beta}\right)$$

Solving the emission and absorption energy equations,  $z = 3.9543$

From equation 1,

$$\cos(3.9543) + \beta \frac{\sin(3.9543)}{3.9543} = -1$$

$$\beta = 1.702$$

#### 4.7.2 $\beta$ for IRMOF-10 (Zn-BPDC MOF)

For Zn-BPDC MOF,  $\lambda_{absorption} = 281 \text{ nm}$  and  $\lambda_{emission} = 352 \text{ nm}$

$$E_{emission} = \frac{hc}{\lambda_{emission}} = \frac{1240 \text{ eVnm}}{352 \text{ nm}} = 3.523 \text{ eV}$$

$$E_{absorption} = \frac{hc}{\lambda_{absorption}} = \frac{1240 \text{ eVnm}}{281 \text{ nm}} = 4.413 \text{ eV}$$



From equation 2 and 3:

For  $E_{emission}$ .

$$3.523 = \left(\frac{\pi^2}{2a}\right)\left(\frac{\alpha}{\beta}\right)$$

For  $E_{absorption}$ .

$$4.413 = \left(\frac{z^2}{2a}\right)\left(\frac{\alpha}{\beta}\right)$$

Solving the emission and absorption energy equations,  $z = 3.5161$

From equation 1,

$$\cos(3.5161) + \beta \frac{\sin(3.5161)}{3.5161} = -1$$

$$\beta = 0.666$$

#### 4.7.3 $\beta$ for IRMOF-1 (Zn-BDC MOF)

For Zn-BDC MOF,  $\lambda_{absorption} = 240 \text{ nm}$  and  $\lambda_{emission} = 379 \text{ nm}$

$$E_{emission} = \frac{hc}{\lambda_{emission}} = \frac{1240 \text{ eVnm}}{379 \text{ nm}} = 3.272 \text{ eV}$$

$$E_{absorption} = \frac{hc}{\lambda_{absorption}} = \frac{1240 \text{ eVnm}}{240 \text{ nm}} = 5.167 \text{ eV}$$

From equation 2 and 3:

For  $E_{emission}$ .

$$3.272 = \left(\frac{\pi^2}{2a}\right)\left(\frac{\alpha}{\beta}\right)$$

For  $E_{absorption}$ .

$$5.167 = \left(\frac{z^2}{2a}\right)\left(\frac{\alpha}{\beta}\right)$$

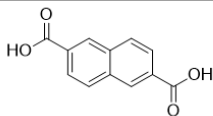
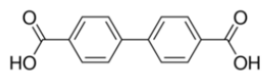
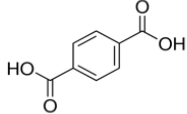
Solving the emission and absorption energy equations,  $z = 3.9479$

From equation 1,

$$\cos(3.9479) + \beta \frac{\sin(3.9479)}{3.9479} = -1$$

$$\beta = 1.684$$

Table 4:  $\epsilon$  &  $\beta$  Values of IRMOFs

MOFs	Ligand	Ligand Structure	$\epsilon$	$\beta$
Zn-NDC	2,6- Naphthalene dicarboxylic acid		2.919	1.702
Zn-BPDC	Biphenyl-4,4'-dicarboxylic acid		2.529	0.666
Zn-BDC	Benzene- 1, 4-dicarboxylic acid		2.477	1.684

From the table, the dielectric constant values of MOFs decrease when the ligands' length is becoming shorter. But  $\beta$  values are not following the trend as it depends on the absorption and emission peaks. The emission peak for Zn-BPDC MOF is at the shorter wavelength than the other two. Thus, the  $\beta$  value is lower for Zn-BPDC MOF.

#### 4.8 Mapping Energy Band Structures for IRMOFs

##### 4.8.1 Predicting Energy Band Structures Considering Only Metal Nodes

We have already calculated  $\beta$  values for three different MOFs. Now, we can predict the energy band diagram for the 1D array of IRMOFs considering only metal nodes.

Now plotting of  $f(z)$  vs  $z$  in equation 1, when  $\beta=1.702$  for IRMOF-8

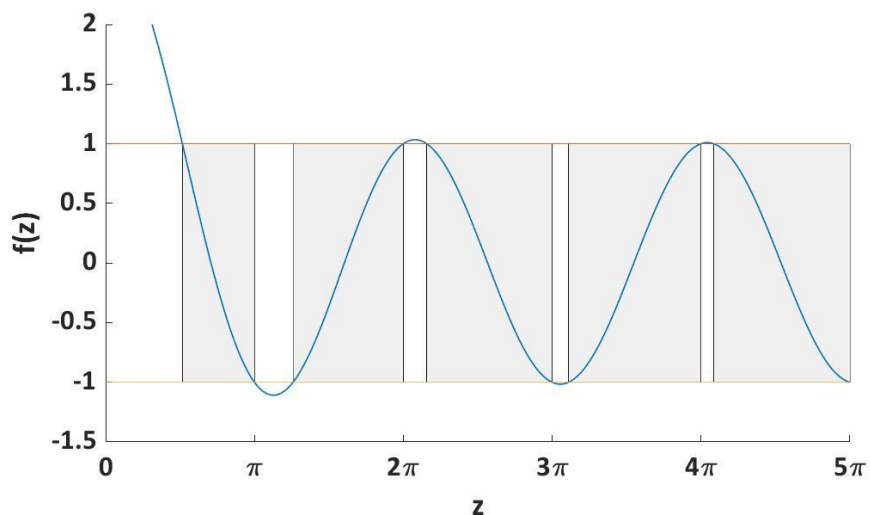


Figure 24: Energy Bands of IRMOF-8 Without Considering Organic Part

Here grey regions are denoting energy bands, and white regions between two allowed bands represent band gaps.

Now plotting of  $f(z)$  vs  $z$  in equation 1, when  $\beta=0.666$  for IRMOF-10

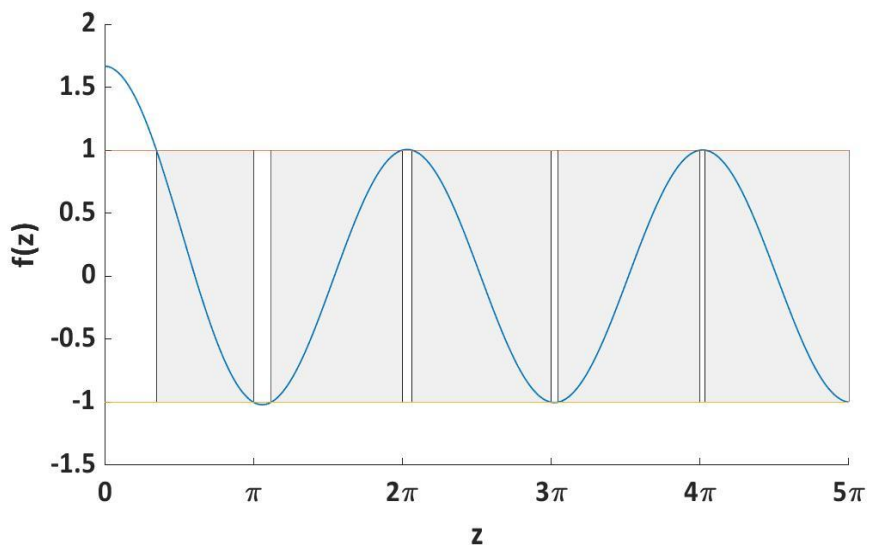


Figure 25: Energy Bands of IRMOF-10 Without Considering Organic Part

Now plotting of  $f(z)$  vs  $z$  in equation 1, when  $\beta=1.684$  for IRMOF-1

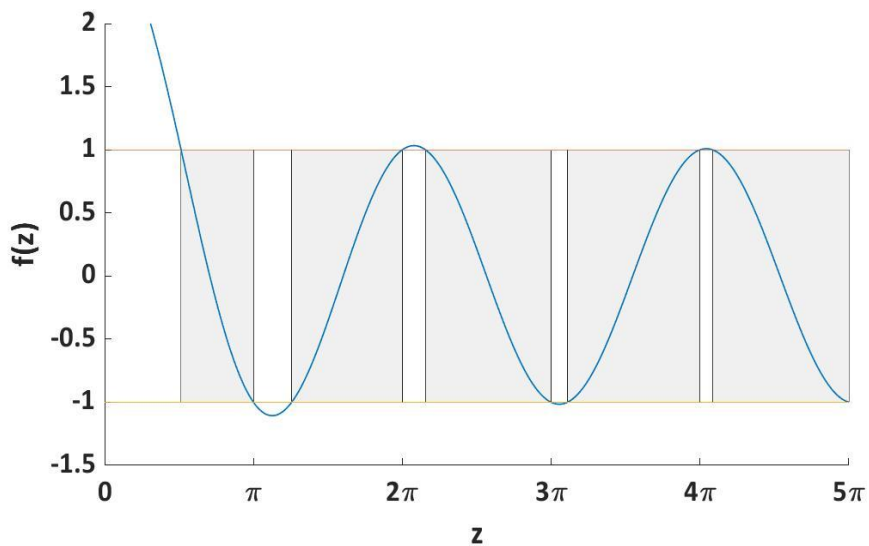


Figure 26: Energy Bands of IRMOF-1 Without Considering Organic Part

#### 4.8.2 Mapping Energy Band Structures with the Impact of Organic Parts

We calculate new values of  $\beta$  to plot the energy band diagram for the 1D array of all 3 MOFs considering the organic parts.

Table 5:  $\beta$  for All IRMOFs Considering the Organic Parts

<b>IRMOFs</b>	<b>Dielectric Constant, <math>\epsilon</math></b>	<b><math>\beta</math> considering only metal nodes</b>	<b><math>\beta</math> considering both metal nodes and ligands, <math>\beta_{new} = \epsilon * \beta</math></b>
Zn-BDC MOF (IRMOF-1)	2.477	1.684	4.171
Zn-NDC MOF (IRMOF-8)	2.919	1.702	4.968
Zn-BPDC MOF (IRMOF-10)	2.529	0.666	1.685

Solution of Schrödinger's equation in region  $0 < x < a$  in Bloch condition for  $\beta_{new}$

$$f(z) = \cos z + \beta_{new} \frac{\sin z}{z} \quad (4)$$

Now plotting of  $f(z)$  vs  $z$  in equation 4, when  $\beta_{new} = 4.968$  for IRMOF-8

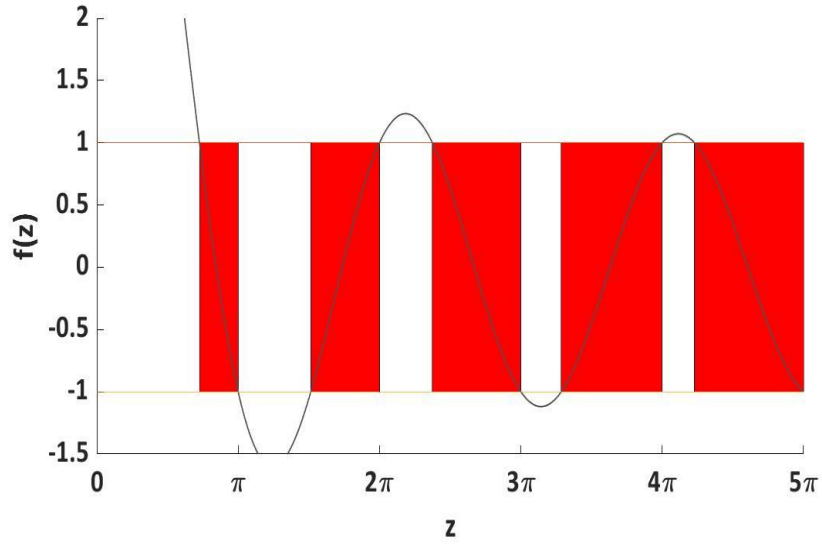


Figure 27: Energy Bands of IRMOF-8 Considering Organic Part (Dielectric Substance)

Here, red regions denote energy bands, and white regions between two allowed bands represent band gaps.

Now plotting of  $f(z)$  vs  $z$  in equation 4, when  $\beta_{\text{new}} = 1.685$  for IRMOF-10

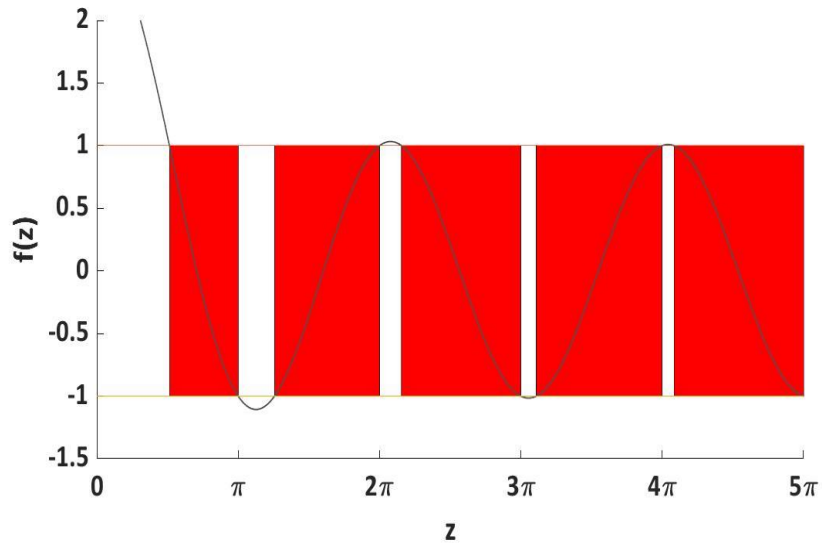


Figure 28: Energy bands of IRMOF-10 Considering Organic Part (Dielectric Substance)

Now plotting of  $f(z)$  vs  $z$  in equation 4, when  $\beta_{\text{new}} = 4.171$  for IRMOF-1

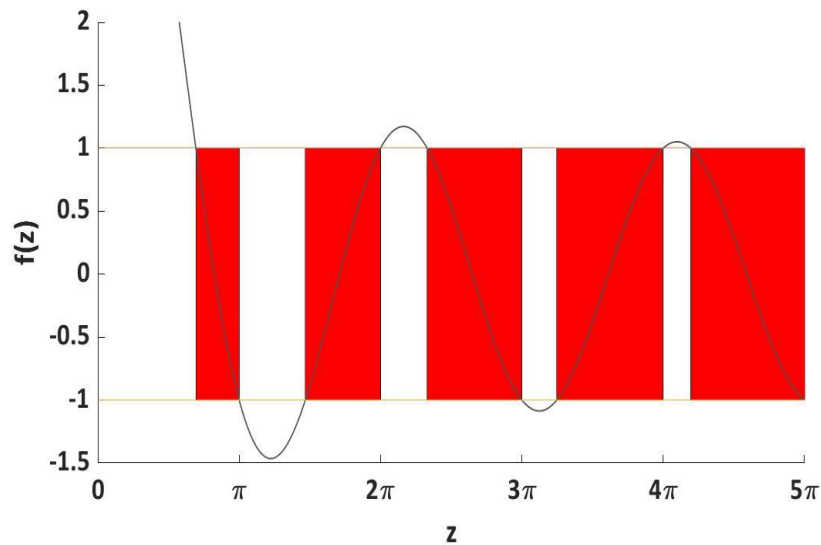


Figure 29: Energy bands of IRMOF-1 Considering Organic Part (Dielectric Substance)

#### ***4.9 Energy Band Diagrams for IRMOFs***

From the previous measurements and calculations, comparison of allowed bands for only metal nodes and metal with organic parts are figured from MATLAB programming.

##### **4.9.1 IRMOF-8**

Now plotting of  $f(z)$  vs  $z$  in equation 1 and 4, when  $\beta = 1.702$  &  $\beta_{\text{new}} = 4.968$

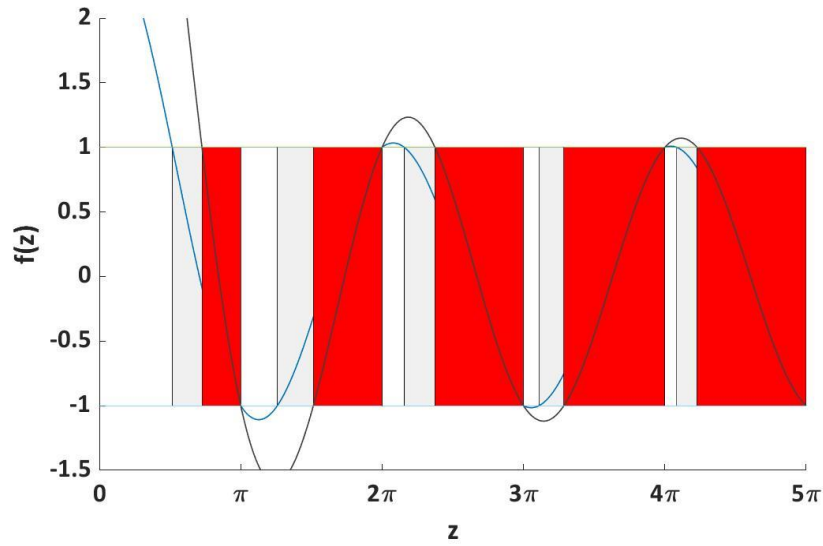


Figure 30: Energy Band Diagram for IRMOF-8

Here, grey parts are the hypothetical energy band regions considering only metal nodes ( $\beta= 1.702$ ), and red parts are the energy band regions considering both metal nodes and organic parts ( $\beta_{\text{new}}= 4.968$ ). After considering organic parts, allowed bands decrease (only red areas), and band gaps increase.

#### 4.9.2 IRMOF-10

Now plotting of  $f(z)$  vs  $z$  in equation 1 and 4, when  $\beta= 0.666$  &  $\beta_{\text{new}} = 1.685$



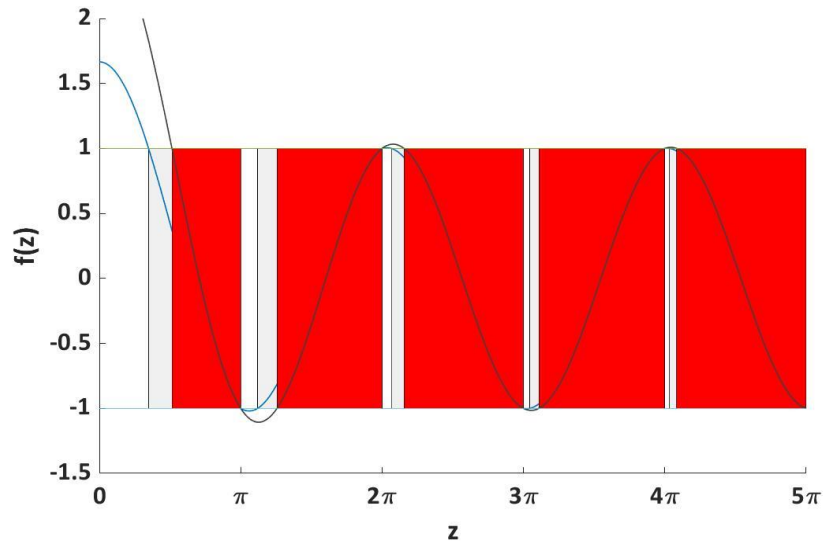


Figure 31: Energy Band Diagram for IRMOF-10

Here, grey parts are the hypothetical energy bands considering only metal nodes ( $\beta = 0.666$ ), and red parts are the energy bands considering both metal nodes and organic parts ( $\beta_{\text{new}} = 1.685$ )

### 4.9.3 IRMOF-1

Now plotting of  $f(z)$  vs  $z$  in equation 1 and 4, when  $\beta = 1.684$  &  $\beta_{\text{new}} = 4.171$

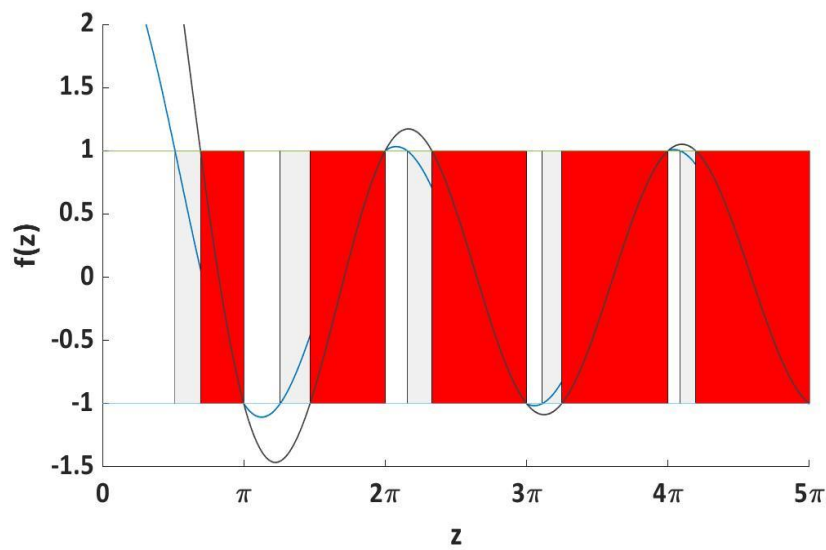


Figure 32: Energy Band Diagram for IRMOF-1

Here grey parts are the hypothetical energy bands considering only metal nodes ( $\beta= 1.684$ ), and red parts are the energy bands considering both metal nodes and organic parts ( $\beta_{\text{new}} = 4.171$ )

#### 4.10 Energy Curves

E vs  $\kappa a$  curves are plotted considering the organic part of IRMOFs for different  $\beta_{\text{new}}$  values from MATLAB programming where the x-axis is  $\kappa a$ .

##### 4.10.1 Calculations for Energy Curve

$$\cos(\kappa a) = \cos z + \beta \frac{\sin z}{z}$$

$$(\kappa a) = \left\{ \cos^{-1} \left( \cos z + \beta \frac{\sin z}{z} \right) \right\}$$

For allowed band Energy,  $E = \frac{(\kappa a)^2}{\pi^2}$

$$E = \frac{h^2 \kappa^2}{2m} = \frac{h^2 \kappa^2 a^2}{2ma^2} = \frac{h^2 (\kappa a)^2}{2ma^2} = \frac{h^2}{2ma^2} \left\{ \cos^{-1} \left( \cos z + \beta \frac{\sin z}{z} \right) \right\}^2$$

##### 4.10.2 E vs $\kappa a$ for Showing Allowed Energy Bands

Now, we are plotting E vs  $\kappa a$  curves for all  $\beta$  values in a single plotting to compare the jumps between two allowed bands for the 1D array of 3 types of MOFs

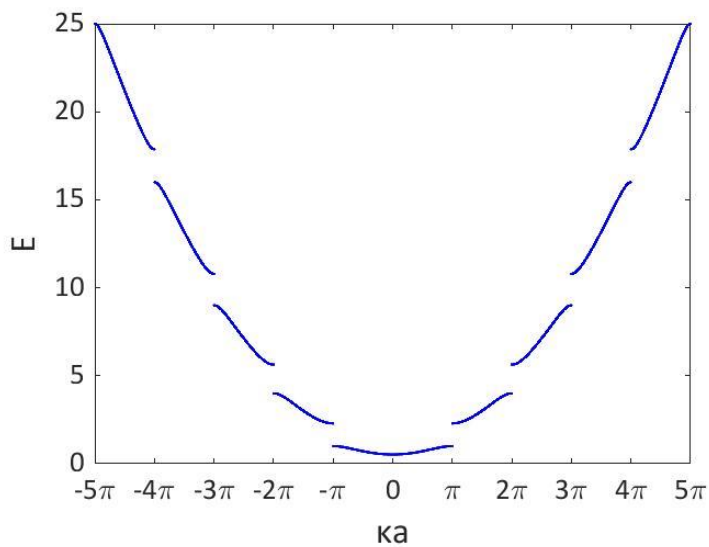


Figure 33: Energy Curve for IRMOF-8

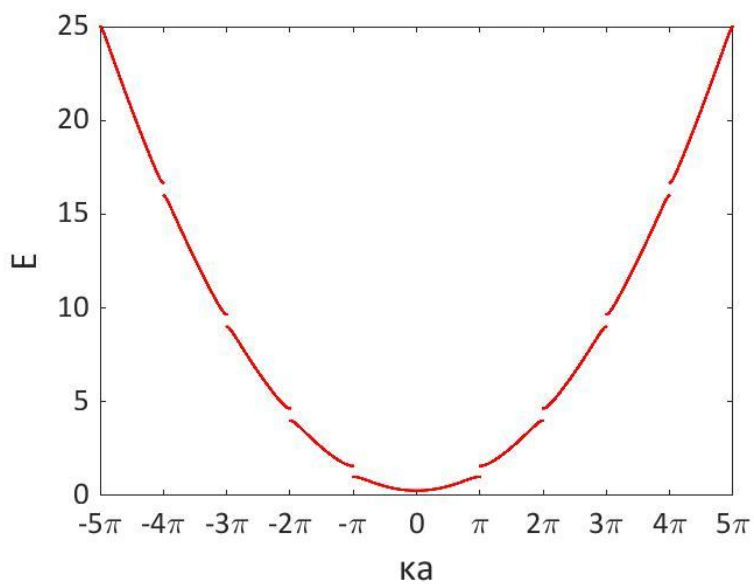


Figure 34: Energy Curve for IRMOF-10

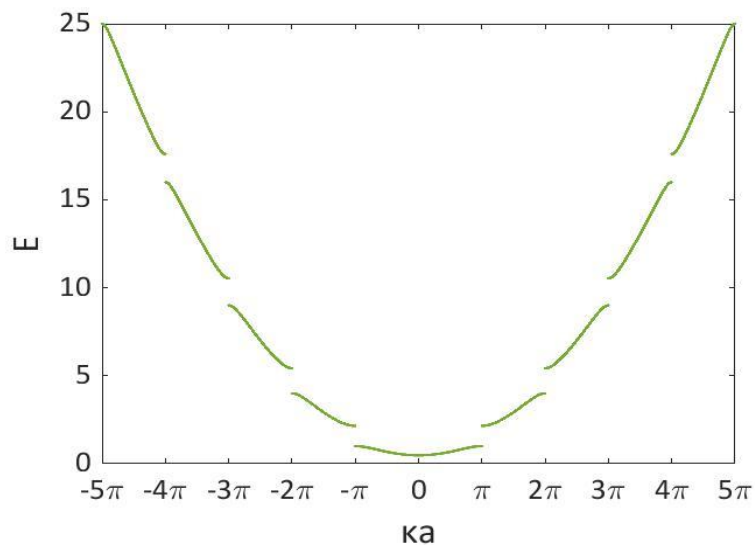


Figure 35: Energy Curve for IRMOF-1

We compare  $E$  vs  $ka$  curves in figure 33 to compare the jumps between two allowed bands for different IRMOFs.

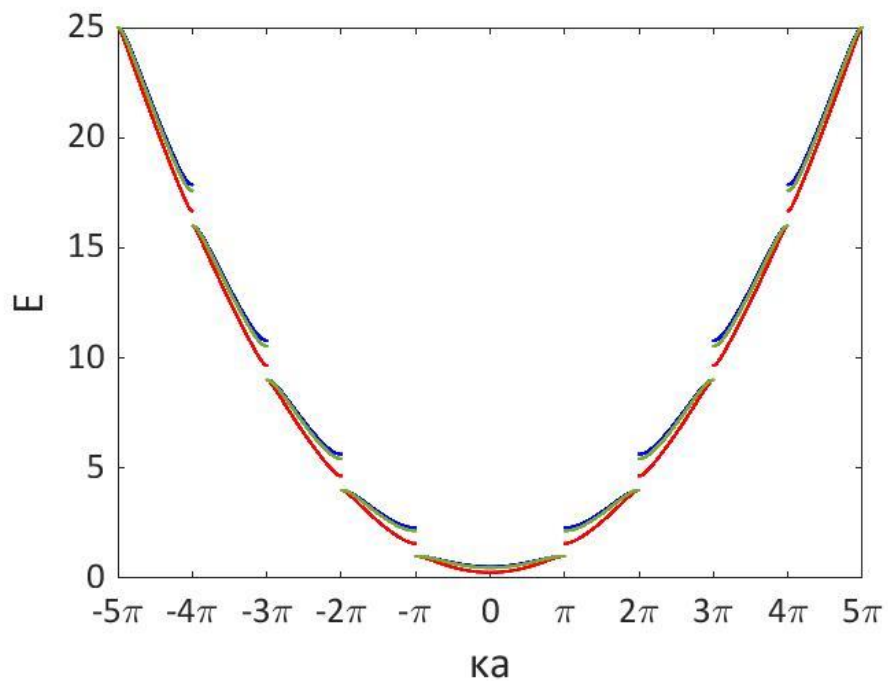


Figure 36: Comparing Energy Curves (Blue: IRMOF-8, Green: IRMOF-1, Red: IRMOF-10)

From the amplitude of the potentials directly calculated from optical energies and solution of Schrodinger equation in Bloch condition, we got the virtual energy band diagrams for the 1D array of all IRMOFs considering only metal nodes. Energy bands become narrower, and band gaps become broader in energy band diagrams for a 1-D array of MOFs after considering the organic parts and dielectric constants. From the energy curves of the 1-D array of Zn-MOFs, it could be concluded that jump from one allowed band to another one, bandgap, is maximum for IRMOF-8, whereas, for IRMOF-10, it is minimum as this jump depends on the  $\beta$  values, which are changing because of the length of ligands and the absorption and emission energy.

## CHAPTER V: CONCLUSION

In conclusion, a series of isorecticular MOFs (IRMOF-1, 8, and 10) were synthesized utilizing the modified solvothermal method. Here materials composition, crystallinity, morphology, dielectric properties, photophysical properties, and thermal stabilities of these three IRMOFs are revealed using different characterization techniques. We found the relationship between the organic subunits' conjugation length and dielectric properties for corresponding IRMOFs. The capacitance (in nF) and the value of dielectric constant for IRMOFs increase for the longer length of Zn-MOFs' ligands. The photoluminescence properties of IRMOFs in different polar solvents exhibit either solvent-driven LMCT emission or ligand-based emission. But it shows only the ligand-centered emission in solid-state because of the interpenetrated and rigid arrangement of dicarboxylic acid chromophores within the IRMOF structure and localized electron density of both the metal nodes and linkers. We observed that solvent type, solvation, and polarity affect the charge transfer dynamics of the IRMOFs in different solutions from the PL analysis. Future studies can explore the effect of solvation dynamics on the charge transfer process in the series of IRMOFs. Different IRMOFs may be utilized as a versatile photosensitizer for molecular electronics, light-energy conversion, or photonic devices, which will provide a potential new area of research in the field of photophysics. Here, energy bands become narrower, and band gaps become broader in energy band diagrams for a 1-D array of MOFs after considering the organic parts. From the energy curves of the 1-D array of three IRMOFs, it could be concluded that dielectric constants and the jump from one allowed band to another one, bandgap, is maximum for IRMOF-8 whereas, for IRMOF-10, it is minimum as this jump between two allowed bands depends on the amplitude of potential

and  $\beta$  values, which are changing because of the length of ligands and the absorption and emission energy.

## REFERENCES

- (1) Furukawa, H.; Cordova, K. E.; O’Keeffe, M.; Yaghi, O. M. The Chemistry and Applications of Metal–Organic Frameworks. *Science* (80-. ). **2013**, *341* (6149). <https://doi.org/10.1126/science.1230444>.
- (2) Kuc, A.; Enyashin, A.; Seifert, G. Metal–Organic Frameworks: Structural, Energetic, Electronic, and Mechanical Properties. *J. Phys. Chem. B* **2007**, *111* (28), 8179–8186. <https://doi.org/10.1021/jp072085x>.
- (3) Lin, C.-K.; Zhao, D.; Gao, W.-Y.; Yang, Z.; Ye, J.; Xu, T.; Ge, Q.; Ma, S.; Liu, D.-J. Tunability of Band Gaps in Metal–Organic Frameworks. *Inorg. Chem.* **2012**, *51* (16), 9039–9044. <https://doi.org/10.1021/ic301189m>.
- (4) Chavan, S.; Vitillo, J. G.; Gianolio, D.; Zavorotynska, O.; Civalleri, B.; Jakobsen, S.; Nilsen, M. H.; Valenzano, L.; Lamberti, C.; Lillerud, K. P.; Bordiga, S. H<sub>2</sub> Storage in Isostructural UiO-67 and UiO-66 MOFs. *Phys. Chem. Chem. Phys.* **2012**, *14* (5), 1614–1626. <https://doi.org/10.1039/C1CP23434J>.
- (5) Allendorf, M. D.; Bauer, C. A.; Bhakta, R. K.; Houk, R. J. T. Luminescent Metal–Organic Frameworks. *Chem. Soc. Rev.* **2009**, *38* (5), 1330–1352. <https://doi.org/10.1039/b802352m>.
- (6) Moosavi, S. M.; Nandy, A.; Jablonka, K. M.; Ongari, D.; Janet, J. P.; Boyd, P. G.; Lee, Y.; Smit, B.; Kulik, H. J. Understanding the Diversity of the Metal–Organic Framework Ecosystem. *Nat. Commun.* **2020**, *11* (1), 1–10. <https://doi.org/10.1038/s41467-020-17755-8>.
- (7) Zhang, F.; Wang, Y.; Chu, T.; Wang, Z.; Li, W.; Yang, Y. A Facile Fabrication of Electrodeposited Luminescent MOF Thin Films for Selective and Recyclable Sensing of Nitroaromatic Explosives. *Analyst* **2016**, *141* (14), 4502–4510. <https://doi.org/10.1039/c6an00840b>.
- (8) Lee, J.; Farha, O. K.; Roberts, J.; Scheidt, K. A.; Nguyen, S. T.; Hupp, J. T. Metal–Organic Framework Materials as Catalysts. *Chem. Soc. Rev.* **2009**, *38* (5), 1450–1459. <https://doi.org/10.1039/b807080f>.
- (9) Murray, L. J.; Dinc, M.; Long, J. R. Hydrogen Storage in Metal–Organic Frameworks. *Chem. Soc. Rev.* **2009**, *38* (5), 1294–1314. <https://doi.org/10.1039/b802256a>.
- (10) Li, J. R.; Kuppler, R. J.; Zhou, H. C. Selective Gas Adsorption and Separation in Metal–Organic Frameworks. *Chem. Soc. Rev.* **2009**, *38* (5), 1477–1504. <https://doi.org/10.1039/b802426j>.



- (11) Tranchemontagne, D. J.; Hunt, J. R.; Yaghi, O. M. Room Temperature Synthesis of Metal-Organic Frameworks: MOF-5, MOF-74, MOF-177, MOF-199, and IRMOF-0. *Tetrahedron* **2008**, *64* (36), 8553–8557. <https://doi.org/10.1016/j.tet.2008.06.036>.
- (12) Li, H.; Eddaoudi, M.; O’Keeffe, M.; Yaghi, O. M. Design and Synthesis of an Exceptionally Stable and Highly Porous Metal-Organic Framework. *Nature* **1999**, *402* (6759), 276–279. <https://doi.org/10.1038/46248>.
- (13) Batten, S. R.; Champness, N. R.; Chen, X.; Garcia-martinez, J.; Kitagawa, S.; Öhrström, L.; Keffe, M. O.; Suh, M. P.; Reedijk, J. Terminology of Metal–Organic Frameworks and Coordination Polymers. *Pure Appl. Chem.* **2013**, *85* (8), 1715–1724. <https://doi.org/10.1351/PAC-REC-12-11-20>.
- (14) Seth, S.; Matzger, A. J. Metal – Organic Frameworks: Examples, Counterexamples, and an Actionable De Fi Nition. *Cryst. Growth Des.* **2017**. <https://doi.org/10.1021/acs.cgd.7b00808>.
- (15) Yaghi, O. M. Reticular Chemistry - Construction, Properties, and Precision Reactions of Frameworks. *J. Am. Chem. Soc.* **2016**, *138* (48), 15507–15509. <https://doi.org/10.1021/jacs.6b11821>.
- (16) Yoo, Y.; Varela-Guerrero, V.; Jeong, H. K. Isoreticular Metal-Organic Frameworks and Their Membranes with Enhanced Crack Resistance and Moisture Stability by Surfactant-Assisted Drying. *Langmuir* **2011**, *27* (6), 2652–2657. <https://doi.org/10.1021/la104775d>.
- (17) Xu, W.; Thapa, K. B.; Ju, Q.; Fang, Z.; Huang, W. Heterogeneous Catalysts Based on Mesoporous Metal–Organic Frameworks. *Coord. Chem. Rev.* **2018**, *373* (October), 199–232. <https://doi.org/10.1016/j.ccr.2017.10.014>.
- (18) Reineke, T. M.; Eddaoudi, M.; Moler, D.; O’Keeffe, M.; Yaghi, O. M. Large Free Volume in Maximally Interpenetrating Networks: The Role of Secondary Building Units Exemplified by TB2(ADB)3[(CH3)2SO]4·16[(CH3)2SO]. *J. Am. Chem. Soc.* **2000**, *122* (19), 4843–4844. <https://doi.org/10.1021/ja000363z>.
- (19) Eddaoudi, M. Systematic Design of Pore Size and Functionality in Isoreticular MOFs and Their Application in Methane Storage. *Science (80-. )*. **2002**, *295* (5554), 469–472. <https://doi.org/10.1126/science.1067208>.
- (20) Rowsell, J. L. C.; Millward, A. R.; Park, K. S.; Yaghi, O. M. Hydrogen Sorption in Functionalized Metal–Organic Frameworks. *J. Am. Chem. Soc.* **2004**, *126* (18), 5666–5667. <https://doi.org/10.1021/ja049408c>.
- (21) Xiao, Y. H.; Gu, Z. G.; Zhang, J. Vapor-Assisted Epitaxial Growth of Porphyrin-Based MOF Thin Film for Nonlinear Optical Limiting. *Sci. China Chem.* **2020**, *63* (8), 1059–1065. <https://doi.org/10.1007/s11426-020-9759-6>.

- (22) Yin, W.; Tao, C.; Wang, F.; Huang, J.; Qu, T.; Wang, J. 7Xqlqj Rswlfdo Surshuwllhv Ri 02 ) Edvhg Wklq Ilopv E \ Fkdqjlqj Wkh Oljdaqv Ri 02 ) V. **2017**, No. November.
- (23) Ortiz-Sánchez, J. M.; Bucher, D.; Pierce, L. C. T.; Markwick, P. R. L.; McCammon, J. A. Exploring the Photophysical Properties of Molecular Systems Using Excited State Accelerated Ab Initio Molecular Dynamics. *J. Chem. Theory Comput.* **2012**, *8* (8), 2752–2761. <https://doi.org/10.1021/ct200740r>.
- (24) Mohan, M.; Pangannaya, S.; Satyanarayan, M. N.; Trivedi, D. R. Photophysical and Electrochemical Properties of Organic Molecules: Solvatochromic Effect and DFT Studies. *Opt. Mater. (Amst).* **2018**, *77*, 211–220. <https://doi.org/10.1016/j.optmat.2018.01.031>.
- (25) Dawood, S.; Dorris, A.; Davis, K.; Hammer, N. I.; Rathnayake, H. Synthesis, Characterization, and Photophysics of Self-Assembled Mn(II)-MOF with Naphthalene Chromophore. *J. Phys. Chem. C* **2021**, *125* (1), 792–802. <https://doi.org/10.1021/acs.jpcc.0c09600>.
- (26) Tereshchenko, O. V.; Buesink, F. J. K.; Leferink, F. B. J. An Overview of the Techniques for Measuring the Dielectric Properties of Materials. *2011 30th URSI Gen. Assem. Sci. Symp. URSIGASS 2011* **2011**, 1–4. <https://doi.org/10.1109/URSIGASS.2011.6050287>.
- (27) Mercuri, G.; Giambastiani, G.; Rossin, A. Thiazole- and Thiadiazole-Based Metal-Organic Frameworks and Coordination Polymers for Luminescent Applications. *Inorganics* **2019**, *7* (12), 1–16. <https://doi.org/10.3390/inorganics7120144>.
- (28) Pamei, M.; Puzari, A. Luminescent Transition Metal–Organic Frameworks: An Emerging Sensor for Detecting Biologically Essential Metal Ions. *Nano-Structures and Nano-Objects* **2019**, *19*, 100364. <https://doi.org/10.1016/j.nanoso.2019.100364>.
- (29) Chen, Y.; Wang, D.; Deng, X.; Li, Z. Metal-Organic Frameworks (MOFs) for Photocatalytic CO<sub>2</sub> Reduction. *Catal. Sci. Technol.* **2017**, *7* (21), 4893–4904. <https://doi.org/10.1039/c7cy01653k>.
- (30) Wang, W.; Xu, X.; Zhou, W.; Shao, Z. Recent Progress in Metal-Organic Frameworks for Applications in Electrocatalytic and Photocatalytic Water Splitting. *Adv. Sci.* **2017**, *4* (4). <https://doi.org/10.1002/advs.201600371>.
- (31) Wang, S.; Liu, J.; Zhao, H.; Guo, Z.; Xing, H.; Gao, Y. Electrically Conductive Coordination Polymer for Highly Selective Chemiresistive Sensing of Volatile Amines. *Inorg. Chem.* **2018**, *57* (2), 541–544. <https://doi.org/10.1021/acs.inorgchem.7b02464>.
- (32) Gutiérrez, M.; Martín, C.; Souza, B. E.; van der Auweraer, M.; Hofkens, J.; Tan, J. C. Highly Luminescent Silver-Based MOFs: Scalable Eco-Friendly Synthesis Paving the Way for Photonics Sensors and Electroluminescent Devices. *ChemRxiv* **2020**, 1–29. <https://doi.org/10.26434/chemrxiv.12631994.v1>.

- (33) Butler, K. S.; Pearce, C. J.; Nail, E. A.; Vincent, G. A.; Sava Gallis, D. F. Antibody Targeted Metal-Organic Frameworks for Bioimaging Applications. *ACS Appl. Mater. Interfaces* **2020**, *12* (28), 31217–31224. <https://doi.org/10.1021/acsami.0c07835>.
- (34) Yang, J.; Yang, Y. W. Metal–Organic Frameworks for Biomedical Applications. *Small* **2020**, *16* (10), 1–24. <https://doi.org/10.1002/smll.201906846>.
- (35) Guan, Q. L.; Han, C.; Bai, F. Y.; Liu, J.; Xing, Y. H.; Shi, Z.; Sun, L. X. Bismuth-MOF Based on Tetraphenylethylene Derivative as a Luminescent Sensor with Turn-off/on for Application of Fe<sup>3+</sup> Detection in Serum and Bioimaging, as Well as Emissive Spectra Analysis by TRES. *Sensors Actuators, B Chem.* **2020**, *325* (July), 128767. <https://doi.org/10.1016/j.snb.2020.128767>.
- (36) Deria, P.; Yu, J.; Smith, T.; Balaraman, R. P. Ground-State versus Excited-State Interchromophoric Interaction: Topology Dependent Excimer Contribution in Metal-Organic Framework Photophysics. *J. Am. Chem. Soc.* **2017**, *139* (16), 5973–5983. <https://doi.org/10.1021/jacs.7b02188>.
- (37) Goswami, S.; Ma, L.; Martinson, A. B. F.; Wasielewski, M. R.; Farha, O. K.; Hupp, J. T. Toward Metal-Organic Framework-Based Solar Cells: Enhancing Directional Exciton Transport by Collapsing Three-Dimensional Film Structures. *ACS Appl. Mater. Interfaces* **2016**, *8* (45), 30863–30870. <https://doi.org/10.1021/acsami.6b08552>.
- (38) Son, H. J.; Jin, S.; Patwardhan, S.; Wezenberg, S. J.; Jeong, N. C.; So, M.; Wilmer, C. E.; Sarjeant, A. A.; Schatz, G. C.; Snurr, R. Q.; Farha, O. K.; Wiederrecht, G. P.; Hupp, J. T. Light-Harvesting and Ultrafast Energy Migration in Porphyrin-Based Metal-Organic Frameworks. *J. Am. Chem. Soc.* **2013**, *135* (2), 862–869. <https://doi.org/10.1021/ja310596a>.
- (39) Kent, C. A.; Liu, D.; Ma, L.; Papanikolas, J. M.; Meyer, T. J.; Lin, W. Light Harvesting in Microscale Metal-Organic Frameworks by Energy Migration and Interfacial Electron Transfer Quenching. *J. Am. Chem. Soc.* **2011**, *133* (33), 12940–12943. <https://doi.org/10.1021/ja204214t>.
- (40) Deria, P.; Yu, J.; Balaraman, R. P.; Mashni, J.; White, S. N. Topology-Dependent Emissive Properties of Zirconium-Based Porphyrin MOFs. *Chem. Commun.* **2016**, *52* (88), 13031–13034. <https://doi.org/10.1039/c6cc07343c>.
- (41) Lee, D. Y.; Shinde, D. V.; Yoon, S. J.; Cho, K. N.; Lee, W.; Shrestha, N. K.; Han, S. H. Cu-Based Metal-Organic Frameworks for Photovoltaic Application. *J. Phys. Chem. C* **2014**, *118* (30), 16328–16334. <https://doi.org/10.1021/jp4079663>.
- (42) Li, H. Y.; Wei, Y. L.; Dong, X. Y.; Zang, S. Q.; Mak, T. C. W. Novel Tb-MOF Embedded with Viologen Species for Multi-Photofunctionality: Photochromism, Photomodulated Fluorescence, and Luminescent PH Sensing. *Chem. Mater.* **2015**, *27* (4), 1327–1331. <https://doi.org/10.1021/cm504350q>.

- (43) Wen, L.; Zhou, L.; Zhang, B.; Meng, X.; Qu, H.; Li, D. Multifunctional Amino-Decorated Metal-Organic Frameworks: Nonlinear-Optic, Ferroelectric, Fluorescence Sensing and Photocatalytic Properties. *J. Mater. Chem.* **2012**, *22* (42), 22603–22609. <https://doi.org/10.1039/c2jm34349e>.
- (44) Hu, S.; Lv, L.; Chen, S.; You, M.; Fu, Z. Zn-MOF-Based Photoswitchable Dyad That Exhibits Photocontrolled Luminescence. *Cryst. Growth Des.* **2016**, *16* (12), 6705–6708. <https://doi.org/10.1021/acs.cgd.6b01129>.
- (45) Farahani, Y. D.; Safarifard, V. Highly Selective Detection of Fe<sup>3+</sup>, Cd<sup>2+</sup> and CH<sub>2</sub>Cl<sub>2</sub> Based on a Fluorescent Zn-MOF with Azine-Decorated Pores. *J. Solid State Chem.* **2019**, *275* (March), 131–140. <https://doi.org/10.1016/j.jssc.2019.04.018>.
- (46) Ding, Z.; Tan, J.; Feng, G.; Yuan, Z.; Wu, C.; Zhang, X. Nanoscale Metal-Organic Frameworks Coated with Poly(Vinyl Alcohol) for Ratiometric Peroxynitrite Sensing through FRET. *Chem. Sci.* **2017**, *8* (7), 5101–5106. <https://doi.org/10.1039/c7sc01077j>.
- (47) Tan, H.; Wu, X.; Weng, Y.; Lu, Y.; Huang, Z. Z. Self-Assembled FRET Nanoprobe with Metal-Organic Framework As a Scaffold for Ratiometric Detection of Hypochlorous Acid. *Anal. Chem.* **2020**, *92* (4), 3447–3454. <https://doi.org/10.1021/acs.analchem.9b05565>.
- (48) V. Stavila, A. A. Talin, and M. D. A. MOF-Based Electronic and Opto-Electronic Devices. **2014**.
- (49) Yang, Q.; Zhou, L.; Wu, Y. X.; Zhang, K.; Cao, Y.; Zhou, Y.; Wu, D.; Hu, F.; Gan, N. A Two Dimensional Metal–Organic Framework Nanosheets-Based Fluorescence Resonance Energy Transfer Aptasensor with Circular Strand-Replacement DNA Polymerization Target-Triggered Amplification Strategy for Homogenous Detection of Antibiotics. *Anal. Chim. Acta* **2018**, *1020*, 1–8. <https://doi.org/10.1016/j.aca.2018.02.058>.
- (50) Zhou, J.; Chen, J.; Ge, Y.; Shao, Y. Two-Dimensional Nanomaterials for Förster Resonance Energy Transfer–Based Sensing Applications. *Nanophotonics* **2020**, *0* (0). <https://doi.org/10.1515/nanoph-2020-0065>.
- (51) Yablonovitch, E.; Gmitte, T. J. Photonic Band Structure: The Face-Centered-Cubic Case Employing Nonspherical Atoms. *Phys. Rev. Lett.* **1991**, *67* (17).
- (52) Baimuratov, A. S.; Rukhlenko, I. D.; Turkov, V. K.; Baranov, A. V.; Fedorov, A. V. Quantum-Dot Supercrystals for Future Nanophotonics. *Sci. Rep.* **2013**, *3*. <https://doi.org/10.1038/srep01727>.
- (53) Kumar, A.; Banerjee, K.; Foster, A. S.; Liljeroth, P. Two-Dimensional Band Structure in Honeycomb Metal–Organic Frameworks. *Nano Lett.* **2018**, *18* (9), 5596–5602. <https://doi.org/10.1021/acs.nanolett.8b02062>.

- (54) Pham, H. Q.; Mai, T.; Pham-Tran, N. N.; Kawazoe, Y.; Mizuseki, H.; Nguyen-Manh, D. Engineering of Band Gap in Metal-Organic Frameworks by Functionalizing Organic Linker: A Systematic Density Functional Theory Investigation. *J. Phys. Chem. C* **2014**, *118* (9), 4567–4577. <https://doi.org/10.1021/jp405997r>.
- (55) Gascon, J.; Hernández-Alonso, M. D.; Almeida, A. R.; van Klink, G. P. M.; Kapteijn, F.; Mul, G. Isoreticular MOFs as Efficient Photocatalysts with Tunable Band Gap: An Operando FTIR Study of the Photoinduced Oxidation of Propylene. *ChemSusChem* **2008**, *1* (12), 981–983. <https://doi.org/10.1002/cssc.200800203>.
- (56) Li, J.; Musho, T.; Wu, N. Functionalization of a Metal-Organic Framework Semiconductor for Tuned Band Structure and Catalytic Activity. *J. of The Electrochem. Soc.* **2019**, *166* (5), 3029–3034. <https://doi.org/10.1149/2.0051905jes>.
- (57) Yablonovitch, E. Photonic Band-Gap Structures. *J. Opt. Soc. Am. B* **1993**, *10* (2), 283–295. <https://doi.org/10.1364/JOSAB.10.000283>.
- (58) Yang, L.; Fang, G.; Ma, J.; Ganz, E.; Han, S. S. Band Gap Engineering of Paradigm MOF - 5. **2014**. <https://doi.org/10.1021/cg500243s>.
- (59) Zhang, Q.; Zhang, C.; Cao, L.; Wang, Z.; An, B.; Lin, Z.; Huang, R.; Zhang, Z.; Wang, C.; Lin, W. Förster Energy Transport in Metal-Organic Frameworks Is beyond Step-by-Step Hopping. *J. Am. Chem. Soc.* **2016**, *138* (16), 5308–5315. <https://doi.org/10.1021/jacs.6b01345>.
- (60) Wang, J.; Jiang, M.; Yan, L.; Peng, R.; Huangfu, M.; Guo, X.; Li, Y.; Wu, P. Multifunctional Luminescent Eu(III)-Based Metal-Organic Framework for Sensing Methanol and Detection and Adsorption of Fe(III) Ions in Aqueous Solution. *Inorg. Chem.* **2016**, *55* (24), 12660–12668. <https://doi.org/10.1021/acs.inorgchem.6b01815>.
- (61) You, L. X.; Zhao, B. B.; Liu, H. J.; Wang, S. J.; Xiong, G.; He, Y. K.; Ding, F.; Joos, J. J.; Smet, P. F.; Sun, Y. G. 2D and 3D Lanthanide Metal-Organic Frameworks Constructed from Three Benzenedicarboxylate Ligands: Synthesis, Structure and Luminescent Properties. *CrystEngComm* **2018**, *20* (5), 615–623. <https://doi.org/10.1039/c7ce01773a>.
- (62) Hao, Z.; Song, X.; Zhu, M.; Meng, X.; Zhao, S.; Su, S.; Yang, W.; Song, S.; Zhang, H. One-Dimensional Channel-Structured Eu-MOF for Sensing Small Organic Molecules and Cu<sup>2+</sup> Ion. *J. Mater. Chem. A* **2013**, *1* (36), 11043–11050. <https://doi.org/10.1039/c3ta12270k>.
- (63) Lin, H.; Maggard, P. A. Microporosity, Optical Bandgap Sizes, and Photocatalytic Activity of M(I)-Nb(V) (M = Cu, Ag) Oxyfluoride Hybrids. *Cryst. Growth Des.* **2010**, *10* (3), 1332–1340. <https://doi.org/10.1021/cg9013619>.
- (64) Liu, X. G.; Wang, L. Y.; Zhu, X.; Li, B. L.; Zhang, Y. Structural Versatility of Eight Zinc(II) Coordination Polymers Constructed with a Long Flexible Ligand 1,4-Bis(1,2,4-Triazol-1-Yl)Butane. *Cryst. Growth Des.* **2009**, *9* (9), 3997–4005. <https://doi.org/10.1021/cg900134f>.

- (65) Yue, Q.; Sun, Q.; Cheng, A. L.; Gao, E. Q. Metal-Organic Framework Based on [Zn<sub>4</sub>O(COO)<sub>6</sub>] Clusters: Rare 3D Kagomé Topology and Luminescence. *Cryst. Growth Des.* **2010**, *10* (1), 44–47. <https://doi.org/10.1021/cg901312t>.
- (66) Wang, J.-L.; Wang, C.; Lin, W. Metal–Organic Frameworks for Light Harvesting and Photocatalysis. *ACS Catal.* **2012**, *2* (12), 2630–2640. <https://doi.org/10.1021/cs3005874>.
- (67) Dawood, S.; Yarbrough, R.; Davis, K.; Rathnayake, H. Self-Assembly and Optoelectronic Properties of Isorecticular MOF Nanocrystals. *Synth. Met.* **2019**, *252* (February), 107–112. <https://doi.org/10.1016/j.synthmet.2019.04.018>.
- (68) Hou, Z.; Fu, X.; Liu, Y. Singularity of the Bloch Theorem in the Fluid/Solid Phononic Crystal. **2006**, 1–5. <https://doi.org/10.1103/PhysRevB.73.024304>.
- (69) Griffiths, D. J. Introduction to Quantum Mechanics. 2005.
- (70) Starobin, J. Nanophysics-NAN603  
<http://learn.uncg.edu/courses/nan603/lecture6/panel8.php>.
- (71) Long, L. S.; Ren, Y. P.; Ma, L. H.; Jiang, Y. B.; Huang, R. Bin; Zheng, L. S. A Unique Three-Dimensional Coordination Polymer Constructed from 4,4'-Biphenyldicarboxylate and Zinc(II). *Inorg. Chem. Commun.* **2003**, *6* (6), 690–693. [https://doi.org/10.1016/S1387-7003\(03\)00087-X](https://doi.org/10.1016/S1387-7003(03)00087-X).
- (72) Hawkins, M.; Saha, S.; Ravindran, E.; Rathnayake, H. A Sol-Gel Polymerization Method for Creating Nanoporous Polyimide Silsesquioxane Nanostructures as Soft Dielectric Materials. *J. Polym. Sci. Part A Polym. Chem.* **2019**, *57* (4), 562–571. <https://doi.org/10.1002/pola.29295>.
- (73) Rathnayake, H.; Saha, S.; Dawood, S.; Loeffler, S.; Starobin, J. Analytical Approach to Screen Semiconducting MOFs Using Bloch Mode Analysis and Spectroscopic Measurements. *J. Phys. Chem. Lett.* **2021**, *12* (2), 884–891. <https://doi.org/10.1021/acs.jpcllett.0c03401>.
- (74) RASPA2/IRMOF-1.cif at master · numat/RASPA2 · GitHub  
<https://github.com/numat/RASPA2/blob/master/structures/mofs/cif/IRMOF-1.cif>  
(accessed Apr 2, 2021).
- (75) RASPA2/IRMOF-8.cif at master · numat/RASPA2 · GitHub  
<https://github.com/numat/RASPA2/blob/master/structures/mofs/cif/IRMOF-8.cif>  
(accessed Apr 2, 2021).
- (76) RASPA2/IRMOF-10.cif at master · numat/RASPA2 · GitHub  
<https://github.com/numat/RASPA2/blob/master/structures/mofs/cif/IRMOF-10.cif>  
(accessed Apr 2, 2021).

- (77) Dawood, S.; Yarbrough, R.; Davis, K.; Rathnayake, H. Self-Assembly and Optoelectronic Properties of Isorecticular MOF Nanocrystals. *Synth. Met.* **2019**, *252* (February), 107–112. <https://doi.org/10.1016/j.synthmet.2019.04.018>.
- (78) Orefuwa, S. A.; Yang, H.; Goudy, A. J. Rapid Solvothermal Synthesis of an Isorecticular Metal-Organic Framework with Permanent Porosity for Hydrogen Storage. *Microporous Mesoporous Mater.* **2012**, *153*, 88–93. <https://doi.org/10.1016/j.micromeso.2011.12.036>.
- (79) Rondi, A.; Rodriguez, Y.; Feurer, T.; Cannizzo, A. Solvation-Driven Charge Transfer and Localization in Metal Complexes. *Acc. Chem. Res.* **2015**, *48* (5), 1432–1440. <https://doi.org/10.1021/ar5003939>.
- (80) Bagchi, B.; Jana, B. Solvation Dynamics in Dipolar Liquids. *Chem. Soc. Rev.* **2010**, *39* (6), 1936–1954. <https://doi.org/10.1039/b902048a>.

## APPENDIX A: MATLAB PROGRAMMING

### Finding Energy Bands for IRMOFs

```
function ZincMOFPlot(beta)
syms x
fz = @(x) cos(x) + ((beta.*sin(x))./x);
onePos = @(x) 1*(x.^0);
oneNeg = @(x) -1*(x.^0);
xxx = 0:.01:5*pi;
plot(xxx, fz(xxx), xxx, onePos(xxx), xxx, oneNeg(xxx))
xlabel('z')
ylabel('f(z)')
title('Energy Bands for IRMOF')
axis([0, 5*pi, -1.5, 3])
xticks([0, pi, 2*pi, 3*pi, 4*pi, 5*pi])
xticklabels({'0', '\pi', '2\pi', '3\pi', '4\pi', '5\pi'})
check = 0;
num = 1;
for j = xxx
    if fz(j) <= 1 && fz(j) >= -1 && check == 0
        pos(num) = j;
        check = 1;
        num = num+2;
    end
    if fz(j) >= 1 || fz(j) <= -1 && check == 1
        check = 0;
    end
end
end
for i = 1:2:9
rectangle('Position', [pos(i), -1, ((i+1)*pi/2)-pos(i),
2], 'FaceColor', 'c')
end
shg;
```



## E vs ka curve for IRMOFs

```
clear
clc
xx = 0:.00001:5*pi;
beta = 4.171;
hold on
syms x
fz = @(x) cos(x) + ((beta.*sin(x))./x);
num = 2;
num2 = 0;
num3 = -1;
check = 1;
zz(1) = 0;
for i = xx
    if fz(i) <= 1 && fz(i) >= -1
        if check == 0
            num2 = num2 + pi;
            num3 = num3*-1;
            check = 1;
        end
        shift(num) = num2;
        zz(num) = i;
        num = num+1;
    else
        zz(num) = zz(num-1);
        shift(num) = num2;
        check = 0;
    end
    thing(num) = num3;
end
thing = thing(2:end);
kappa = acos(fz(zz).*thing)+shift-pi;
E=zz.^2 ./ pi^2;
figure(1)
plot(kappa, E, 'b.')
axis([0, 5*pi, 0, 25])
xticks([0,pi,2*pi,3*pi,4*pi,5*pi])
xticklabels({'0', '\pi', '2\pi', '3\pi', '4\pi', '5\pi'})
xlabel('ka')
ylabel('E')
shg;
```